Communication Channel Measurement and Modeling for Inductive Wireless Power Transfer

LOVE ROSÉN
MASTER´S THESIS
DEPARTMENT OF ELECTRICAL AND INFORMATION TECHNOLOGY
FACULTY OF ENGINEERING | LTH | LUND UNIVERSITY

Communication Channel Measurement and Modeling for Inductive Wireless Power Transfer

Love Rosén
lr@nok9.com

Department of Electrical and Information Technology
Lund University
In Collaboration with nok9 and Google

Academic Supervisor: Buon Kiong Lau

Industrial Supervisors: Laurens Swaans
Kiavash Faraji

Examiner: Mats Gustafsson

March 16, 2020

Printed in Sweden
Tryckeriet i E-huset, Lund

Abstract

Wireless Power Transfer (WPT) technology has experienced phenomenal success in the application of wireless charging of smartphones. With the Qi Specification becoming the dominant standard, wireless charging's convenience goes beyond cable-free charging to facilitate interoperability between chargers and devices from different vendors.

For wireless charging to operate correctly, the power transmitter (charger) and the receiver (user device) should communicate with each other. In the current release of the Qi Specification (Rel 1.2.4), the communication is performed in the same frequency band as the power transfer (in-band communication). Therefore, the properties of the in-band channel determine the quality of the communication link. However, since WPT has only become hugely popular in recent years, the in-band channel has not yet attracted a lot of attention.

In this thesis, the focus is to measure and characterize the in-band channel for scenarios of interest to wireless charging. To enable the channel measurement, a custom-designed setup was made, allowing simultaneous measurements of currents and voltages in the transmitter and receiver. Using this setup, the channel has been characterized as a two-port network using Z-parameters. Observations regarding the Z-parameters, as well as the power transfer efficiency, in various situations are presented and discussed. The first harmonic approximation (FHA) based channel model was applied and extended for the analysis of the results.

Major findings of the thesis include: 1) the amplitude of the imaginary part of the Z-parameters is larger than the real part by one to two orders of magnitude in the frequency of interest (80 to 500 kHz), setting a high accuracy requirement of the measurement system, 2) Power transfer ratio behavior is dependent heavily on WPT circuit parameters interacting with the channel parameters, pointing to opportunities for optimization, 3) The effects of ferrites and foreign objects can be included by extending the simple FHA based channel model with additional coil(s) to model eddy current induced inductance change and resistive losses.

Popular Science Summary

In recent years, the use of wireless power transfer (WPT) in mobile devices, like cellphones, has become hugely popular. With companies like Google, Apple and Samsung making use of the technology, WPT is expected to see increased usage not only in cellphones, but in other areas as well, for example in the automotive industry. WPT is in a sense a recent technology. The groundwork was laid in the early 19th century, but practical applications have only become commercially available on large scale in the recent decade.

WPT in its most common form is based on electromagnetic induction between two coils. The magnetic field generated by a transmitting coil threads the receiving coil, which causes a voltage to appear in the receiving coil. This voltage can be used, for example, to charge a cellphone battery, and thus electrical power can be transferred without the use of wires. This thesis work investigates the characteristics of the coil-to-coil power transfer system by making measurements of the voltages and currents in the coils in various different situations. With the use of a custom made measurement setup centered around an oscilloscope, the system has been measured with various distances and alignments between the coils, at various levels of input power and frequency, as well as with nearby metallic objects, so called foreign objects (FOs) or friendly metals (FMs), that can potentially have huge effects on the power transfer.

The results are mainly in the form of Z-parameters, which describe how voltages and currents are affected by the system. The findings show how the Z-parameters, as well as the efficiency of the system, are affected by the environment in which the power transfer is taking place. Attempts have also been made to model the channel through which power is transferred, based on circuit theory. Some of the issues that have come up along the way and insights gained from them during the execution of the study are also presented. It is hoped that the investigation and its results will aid in future studies into the WPT channel.

Acknowledgments

I would like to express my gratitude toward nok9 and Google for allowing me to take on this project and for introducing me to the fascinating world of wireless power.

My most sincere gratitude goes out to my academic supervisor Professor Buon Kiong Lau, who has provided invaluable support and insight, and who through countless discussions has steered me in the right direction. I would also like to thank my industrial supervisors, Laurens Swaans and Kiavash Faraji, for the guidance and expertise they have provided throughout the project.

I also want to thank the wonderful people at nok9 for the support they have given. Thank you Arianna Amaya, Brenda Awuor Odhiambo and Jonatan Nyström for your valuable input and encouragement during the project.

Performing this thesis project would not have been as positive and rewarding an experience as it have been without the aforementioned people.

Table of Contents

List of Figures

List of Tables

List of Acronyms

A/D	Analog to Digital
AC	Alternating Current
DC	Direct Current
FHA	First Harmonic Approximation
FM	Friendly Metal
FO	Foreign Object
FSK	Frequency Shift Keying
LTI	Linear Time Invariant
PA	Power Amplifier
VNA	Vector Network Analyzer
WPC	Wireless Power Consortium
WPT	Wireless Power Transfer

List of Symbols

ω	Angular Frequency
j	Imaginary Unit
k	Coupling Factor
L_p	Primary/Transmitting Coil Self Inductance
L_s	Secondary/Receiving Coil Self Inductance
L_3, L_4	Virtual Coil Inductances
R_s	Primary Coil Resistance
R_p	Secondary Coil Resistance
R_S	Source Resistance
R_L	Load Resistance
C	Capacitance
M_{mn}	Mutual Inductance Between Coils m and n
I_1	Primary Coil Current
I_2	Secondary Coil Current
I_3, I_4	Virtual Coil Current
V_1	Primary Coil Voltage
V_2	Secondary Coil Voltage
V_3, V_4	Virtual Coil Voltage
Z_m	Total Series Impedance for Coil m
Z_{mn}	Z-Parameter (Impedance Parameter)

Chapter 1
Introduction

1.1 Background

Wireless power transfer (WPT) is a technology that has its roots in the early 19th century, and can be traced back to Michael Faraday's demonstration of electromagnetic induction in 1831 [1]. In his experiment, electric current was passed through a coil with a ferromagnetic core, which produced a magnetic field in the core. He showed that if the current, and hence the magnetic field, is time-varying, then an electromotive force is induced in another coil with the same core.

In the late 19th century, Nikola Tesla had a grand vision of applying this principle to transmit electrical power and information over large distances through the air [2]. However, his vision was not realized, due to incorrect theoretical understanding of the physical phenomenon behind WPT.

Since then, WPT has largely become a niche topic with limited practical applications. Early examples of commercially available products using WPT include electric toothbrushes and electric razors, where the use of the technology was motivated by the need to minimize electrical hazards, as the devices are commonly used in wet environments.

Now, in the early 21st century, WPT is becoming an increasingly relevant technology, with various applications ranging from implementations in home electronic devices to medical devices [3]. It serves as a way to bypass wires in cases where their use is impossible, or where they add needless complications to the power transfer situation.

Importantly, it has become common to implement wireless charging in mobile devices as a means to simplify the charging process [4]. Many manufacturers have included wireless charging in their products, with the Qi Specification [5] being the most adopted WPT standard. The Qi standard is developed by the Wireless Power Consortium (WPC) [6], whose membership includes popular brands like Apple, Samsung, and Huawei.

1.2 Motivation

In WPT systems, there is a need for the receiving device to communicate with the transmitting base station. In the Qi standard [5], this is done using the so-called in-band communication, where the data is sent using the same physical channel

as is used for power transfer. There are various reasons why WPT systems would benefit from higher data rates. Functions such as identification and authentication require large amount of data to be transmitted, and establishing communication more rapidly and reliably enhances the end user experience.

To improve the rate of which data is transferred, modulation schemes can be implemented which allows for faster communication for the given circumstances. To find the optimal communication scheme, knowledge about the physical channel is essential. As the transmitting and receiving coils in a wireless power system generally moves independently of each other, the channel is likely to differ to some extent in each power transfer scenario. For instance, a smartphone using Qi charging can be placed on a charging pad with various alignments between the respective coils. Moreover, there can be metal objects such as coins and keys, which are accidentally placed between the smartphone and the charging pad. According to existing studies such as [7], such objects can affect the channel significantly. However, detailed characterization of wireless power channels is not yet available. Therefore, it is both interesting and practically important for this channel to be known and its properties studied.

1.3 Objective

The primary objective of this thesis is to characterize empirically the in-band communication channel for WPT applications. The focus is on practical wireless charging scenarios. To accomplish this, the tasks include:

- Design of a measurement setup for in-band channels, including relevant measurement scenarios.
- Measurement of in-band channels for different scenarios and parameters of interest.
- Mathematical modeling of in-band channels, allowing for future link and system level studies.

The first task concerned literature survey, preparatory research and simulations, as well as design and setup of the measurement system. This task took the longest time since there exists no dedicated method or equipment to perform inductive WPT channel measurement for typical usage scenarios. Moreover, to streamline data collection for many measurement scenarios of interest, significant effort was put into automating the measurement process.

1.4 Structure

This thesis is organized in the following way. First, this introductory chapter (*Chapter 1: Introduction*) describes the background and motivation for the thesis project. This is followed by a chapter *(Chapter 2: Theoretical Framework)* describing the theoretical framework on which the project is based, including the theoretical background to inductive power transfer. The subsequent chapter (*Chapter 3: Methodology*) details how the project was carried out and the methodology that

was used. Moreover, it describes the equipment and tools that were utilized in the project. The results, with analysis and discussion, are presented in the following chapter (*Chapter 4: Results*). Finally, conclusions and suggestions for future work are given (*Chapter 5: Conclusions and Future Work*).

Chapter 2
Theoretical Framework

This chapter provides the theoretical framework for inductive WPT systems, describing key concepts in ideal as well as practical systems that are important for understanding inductive WPT channels and their properties.

2.1 Self Inductance

A current running through a coil gives rise to a magnetic field according to Ampere's circuital law [8]. The magnetic flux generated by a single isolated coil will also pass through the coil itself. Faraday's law of electromagnetic induction teaches us that when a coil is subjected to a time varying magnetic field, it causes a voltage to be induced over the terminals. The voltage will be induced as to oppose the change in magnetic flux, as described by Lenz's law [9]. An alternating current (AC) through a coil will thus generate a magnetic field which impedes the current running through it. The impedance Z in the frequency domain is described by

$$Z(\omega) = j\omega L \ [\Omega], \tag{2.1}$$

where ω is the angular frequency, L is the self inductance of the coil. The impedance Z is a measure of how the coil opposes the change in current by generating a magnetic field; and j is the imaginary unit.

2.2 Mutual Inductance

The magnetic field generated by the current flowing through one coil (the primary or transmitting coil) can be linked to another coil (the secondary or receiving coil) [8]. When the two coils are aligned such that the time varying magnetic field generated by one coil is passing through the other, a voltage is induced in the receiving coil [9]. Should the receiving coil be connected to some closed circuit, the voltage can be used to drive a current through a connected load.

The mutual inductance M between two coils relates the magnitude of the voltage induced in one coil V_s (secondary coil) to the time-varying current I_p flowing through the other (primary coil). If the secondary coil is open circuited, then the voltage across the secondary coil terminal (in frequency domain) is given by

$$V_s = Z_M(\omega) I_p \text{ [V]}, \tag{2.2}$$

where

$$Z_M(\omega) = j\omega M \text{ [}\Omega\text{]}. \tag{2.3}$$

To define a unitless coupling factor k that quantifies the degree of inductive coupling, M can also be expressed as

$$M = k\sqrt{L_p L_s} \text{ [H]}, \tag{2.4}$$

which is a function of both coils' self inductances, L_p and L_s, where L_p is the self inductance of the primary coil, and L_s of the secondary coil. The coupling factor k is a measure of how much of the magnetic flux generated by one coil links to the other coil [10]. k can take on a value between 0 and 1. A value of 1 means the coils are perfectly coupled and there is no leakage flux, which is in reality unobtainable. In WPT systems, k is highly dependent on the distance between and the relative alignment of the coils. A high coupling factor is achieved in transformers by introducing a common ferromagnetic core to the coils. In WPT systems, however, it is inconvenient to do so since the transmitting and receiving coils are located in separate devices that do not share a common core.

2.3 Resonance in WPT Systems

As a coil inherently has finite self inductance, the current in the coil circuit is naturally impeded. To obtain power transfer without an unreasonably high voltage input, resonance can be introduced into the system [11].

On each of the transmitting and receiving side, a capacitor can be introduced, as shown in Figure 2.1, such that the total series impedance becomes very low. The reactances resulting from the capacitance (C) and inductance (L) can for a given frequency, the so-called resonance frequency, cancel out each other, leaving only the resistances (source resistance R_S or load resistance R_L) as the sole contributor to impedance.

WPT as described in the Qi Specification uses resonance on both the transmitting and receiving sides. Resonance frequency on each side calculated in a series resistor-inductor-capacitor (RLC) circuit using the following equation:

$$f_r = \frac{1}{2\pi}\sqrt{\frac{1}{LC}} \text{ [Hz]}. \tag{2.5}$$

To obtain the resonance frequency of the two-coil circuit in Figure 2.1, L and C in (2.5) are replaced by equivalent series inductance and capacitance as seen by the source. Resonance allows for an induced voltage to generate a relatively large current, providing power to the load according to $P = I_s^2 \cdot R_L$, where I_s is the current in the secondary coil. An example of how the power transferred to the load (in a two-coil circuit) is affected by frequency for a given voltage input, is shown in Figure 2.2. The system achieves maximum power transfer at around 115 kHz. On either side of the resonance peak, the impedance becomes increasingly large due

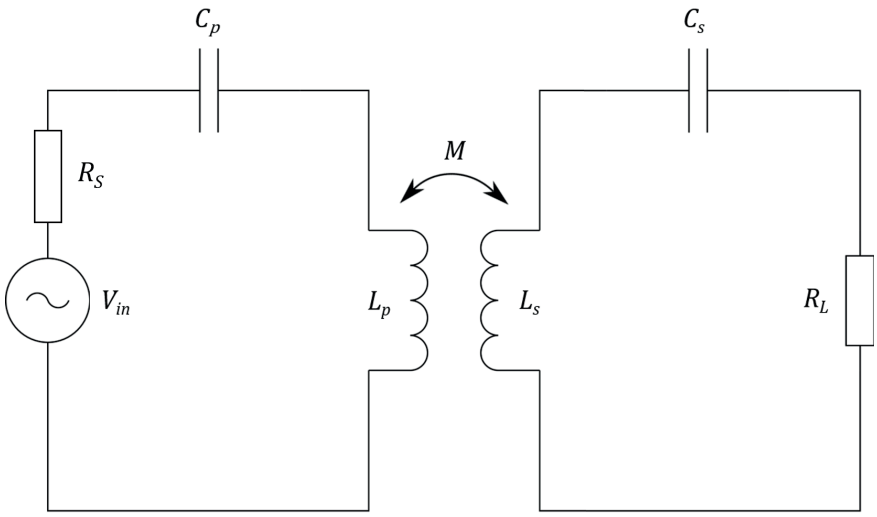

Figure 2.1: Circuit schematic of WPT system including resonance capacitors. Ideal circuit elements are assumed.

to increasing reactance caused by either the capacitance (lower than resonance) or inductance (higher than resonance) dominating the total reactance.

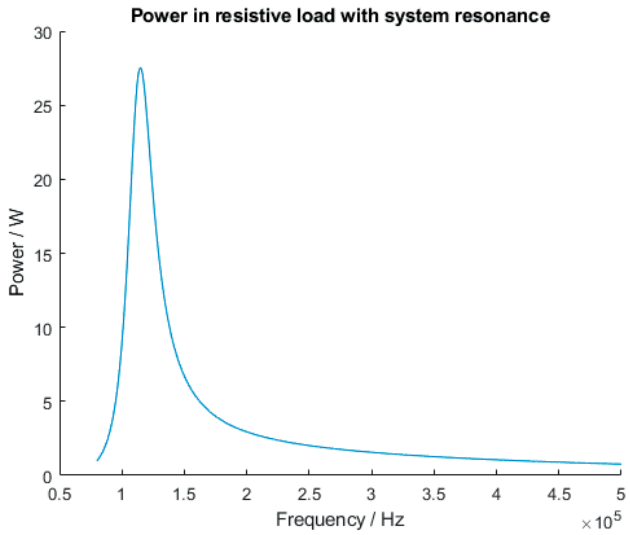

Figure 2.2: Power consumed in the load for a constant voltage input (V_{in}) of 10 V, when resonance is present at both the receiving and transmitting sides. The results are based on the first harmonic approximation model described in Section 2.4.

Parameter	Value
V_{IN}	10 V
L_P	15.4 μH
L_S	15.3 μH
C_P	0.1 μF
C_S	0.1 μF
k	0.9
R_L	20 Ω

2.4 First Harmonic Approximation Model

Figure 2.3 shows the first harmonic approximation (FHA) model used to predict the behavior of a WPT coil system. The model is based on the fact that the induced voltage can be modeled as a current driven voltage source [12]. The magnitude of the induced voltages in the primary and secondary coils, respectively, depends on the current on the opposite side, i.e., I_2 and I_1, as well as on the mutual inductance, M. Using basic circuit theory, a set of equations can be established to describe the coil system:

$$V_1 = j\omega L_p I_1 + j\omega M I_2 + R_p I_1 \text{ [V]}, \tag{2.6}$$

$$V_2 = j\omega L_s I_2 + j\omega M I_1 + R_s I_2 \text{ [V]}, \tag{2.7}$$

$$I_1 = \frac{V_{IN} Z_2}{Z_1 Z_2 + \omega^2 M^2} \text{ [A]}, \tag{2.8}$$

$$I_2 = \frac{-V_{IN} j\omega M}{Z_1 Z_2 + \omega^2 M^2} \text{ [A]}. \tag{2.9}$$

In these equations, ω is the angular frequency and j is the imaginary unit. The

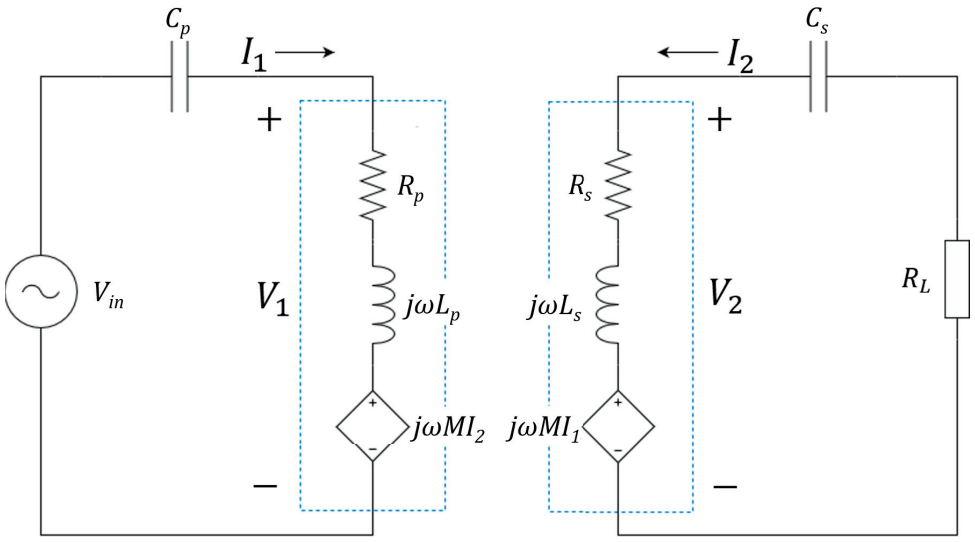

Figure 2.3: Circuit theory model of the WPT system shown in Figure 2.1. The dashed lines mark the physical boundaries of the primary and secondary coils.

voltages V_1 and V_2 are the voltages over the primary and secondary coils, respectively. I_1 and I_2 are the primary and secondary side currents, respectively. Z_1 and Z_2 are the total series impedances on the primary and secondary sides, respectively. The total impedance Z_1 on the primary side consists of the primary coil self inductance L_p, the resonance capacitance C_p, and the coil resistance R_p. Z_2 consists of the secondary coil self inductance L_s, the resonance capacitance C_s,

the coil resistance R_s as well as the load resistance R_L. The impedances are given by:

$$Z_1 = j\omega L_p + \frac{1}{j\omega C_p} + R_p \ [\Omega], \tag{2.10}$$

$$Z_2 = j\omega L_s + \frac{1}{j\omega C_s} + R_s + R_L \ [\Omega]. \tag{2.11}$$

An expanded version of the FHA model, including additional coils, is described in Section 2.6.

2.5 Eddy Currents

Currents can be generated in a metal object, if the object is subject to an external alternating magnetic field [9]. This phenomenon occurs when a voltage is induced in the metal object, similarly to the current induced in a coil, such that the current travels in a closed loop in the metal object. Due to the resistance in the metal, the current can cause the metal object to heat up, thus consuming power.

In WPT scenarios, especially for the charging of small devices, metallic items (termed "FOs") such as coins and keys may be found in close proximity to the inductive coils, and thus are subjected to significant alternating magnetic field. In addition, the transmitting or receiving device may contain metals within itself (termed "friendly metals"). As the eddy currents can cause power to be consumed in locations other than the load, there will be a mismatch between the power sent by the transmitting coil and the power received by the receiving coil. Additionally, the eddy currents generate their own magnetic field, which impacts the equivalent self inductances and the mutual inductance of the coil system, as seen across the coil terminals. As the additional magnetic field affects the voltage induced in the transmitting and receiving coils, the apparent self inductance of the coils is changed as a result.

2.6 Extended FHA Model

The basic FHA model described in Section 2.4 does not include everything that can realistically be expected to affect the WPT system. The generation of eddy currents in nearby objects imposes potential power losses which are not represented in the model. To include these effects, an extended version of the FHA model is proposed, which is expanded to include additional coils, approximating eddy currents. A system with two additional coils is shown in Figure 2.4, in which the additional coils can be used to represent eddy currents in, for example, the ferrite material attached to the transmitting and receiving coils. The additional virtual coils are each represented by an inductance (L_3 or L_4), a resistance (R_3 or R_4), as well as a voltage source with a generated voltage related to the mutual inductance between the virtual coil and each of the other coils.

The voltages of the system are described by the following matrix equation:

$$\begin{bmatrix} V_1 \\ V_2 \\ V_3 \\ V_4 \end{bmatrix} = \begin{bmatrix} L_P & M_{12} & M_{13} & M_{14} \\ M_{21} & L_S & M_{23} & M_{24} \\ M_{31} & M_{32} & L_3 & M_{34} \\ M_{41} & M_{42} & M_{43} & L_4 \end{bmatrix} \begin{bmatrix} I_1 \\ I_2 \\ I_3 \\ I_4 \end{bmatrix} \text{ [V]}, \tag{2.12}$$

in which M_{mn} is the mutual inductance between coils m and n. Further, M_{mn} is equal to M_{nm} by reciprocity in a linear time invariant (LTI) system. The currents in the system are given by

$$I_1 = \frac{V_{IN} - I_2 j\omega M_{12} - I_3 j\omega M_{13} - I_4 j\omega M_{14}}{Z_1} \text{ [A]}, \tag{2.13}$$

$$I_2 = \frac{-I_1 j\omega M_{21} - I_3 j\omega M_{23} - I_4 j\omega M_{24}}{Z_2} \text{ [A]}, \tag{2.14}$$

$$I_3 = \frac{-I_1 j\omega M_{31} - I_2 j\omega M_{32} - I_4 j\omega M_{34}}{Z_3} \text{ [A]}, \tag{2.15}$$

$$I_4 = \frac{-I_1 j\omega M_{41} - I_2 j\omega M_{42} - I_3 j\omega M_{43}}{Z_4} \text{ [A]}, \tag{2.16}$$

in which $Z_3 = R_3 + j\omega L_3$ and $Z_4 = R_4 + j\omega L_4$.

Using substitutions, expressions for the primary side currents and source voltage can be obtained. These are presented in the Appendix, Section A.

An appropriate way to assign values to the additional coil parameters, R_3, R_4, L_3 and L_4, as well as the respective mutual inductances, has not been found. It is hoped that these parameters can be given values based on the material properties and geometry of nearby objects in which eddy currents can be induced. It is still interesting, however, to look at how these parameters appear in the expressions for Z-parameters, which is discussed in Section 2.7, as well as in the *Results* chapter (Chapter 4).

2.7 Z-Parameters

Z-parameters, or impedance parameters, are used to describe the relationship between currents and voltages in an electrical network [13], and thus they can be used to represent the input and output relationship of the primary and secondary WPT coils, as depicted in Figure 2.5. In general, these parameters fully describe the WPT channel, which is empirically studied in this thesis. Each Z-parameter gives the contribution to the voltage on one side, from the current on the same or opposite side.

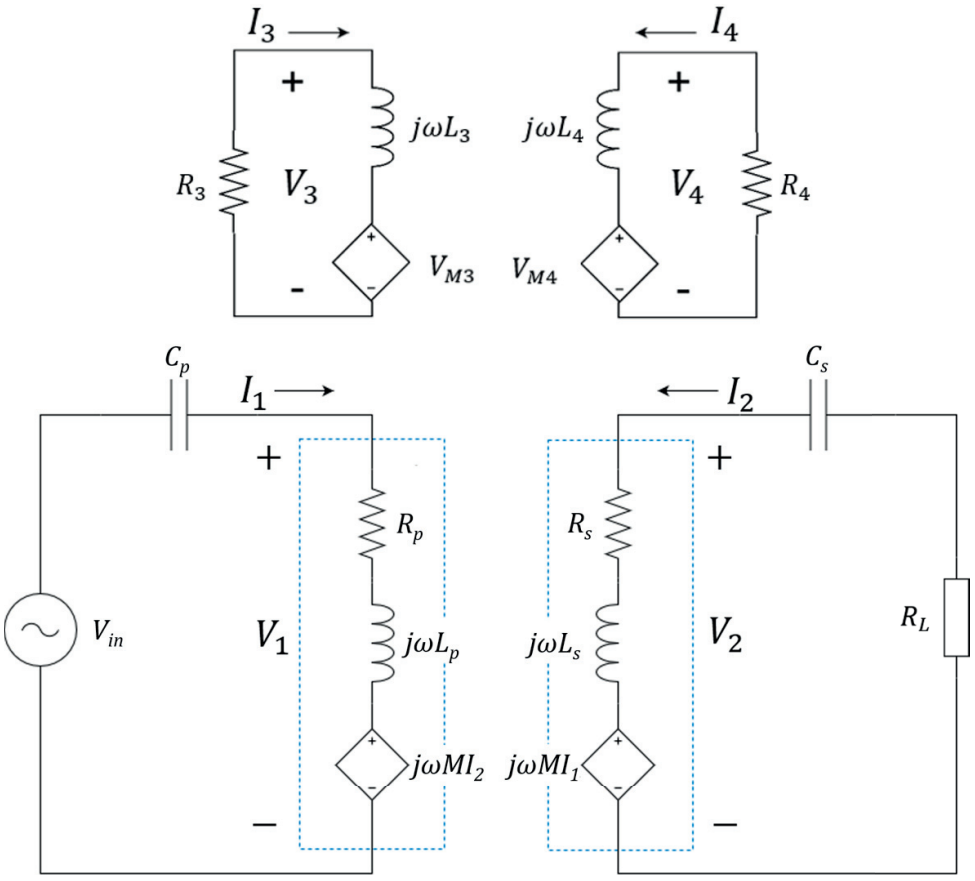

Figure 2.4: Extended FHA model of the WPT system, including two additional coils. The dashed lines mark the physical boundaries of the primary and secondary coils.

The Z-parameter representation for a two-port network is described by two linear equations in a matrix form, as follows:

$$\begin{bmatrix} V_1 \\ V_2 \end{bmatrix} = \begin{bmatrix} Z_{11} & Z_{12} \\ Z_{21} & Z_{22} \end{bmatrix} \begin{bmatrix} I_1 \\ I_2 \end{bmatrix} \quad [\mathrm{V}]. \tag{2.17}$$

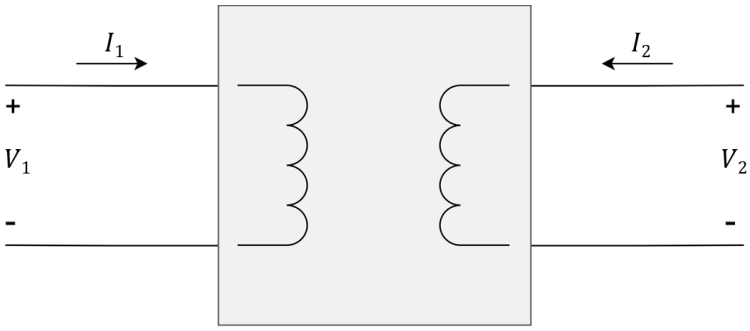

Figure 2.5: Two-port representation of WPT coils.

Using the basic FHA model described in Section 2.4, expressions for the Z-parameters can be obtained:

$$Z_{11} = j\omega L_P + R_P \ [\Omega], \tag{2.18}$$
$$Z_{21} = j\omega M \ [\Omega], \tag{2.19}$$
$$Z_{12} = j\omega M \ [\Omega], \tag{2.20}$$
$$Z_{22} = j\omega L_S + R_S \ [\Omega]. \tag{2.21}$$

Using the model, Z_{11} and Z_{22}, which gives the contribution to the voltage on either side from the current on the same side, have an imaginary part and a real part corresponding to the respective coil's reactance from the self inductance, and internal resistance. Z_{12} and Z_{21} only have a reactive part from the mutual inductance of the system. For LTI systems, Z_{12} and Z_{21} are the same by reciprocity.

Real WPT scenarios are in general more complex than the simple model in Figure 2.3, especially due to ferrite plates that are often attached to the coils, as well as FOs found in the vicinity of the WPT system. Losses in the WPT, e.g., due to eddy currents in FOs, can show up as an increase in the real parts of Z parameters, as any power loss in the channel must be represented as real power consumption. These losses are approximated in the suggested extended model described in Section 2.6, where additional coils are used to model eddy currents. Using this model, the Z-parameters are:

$$\begin{aligned} Z_{11} = \Big[& j\omega^3(L_4M_{13}^2 + L_3M_{14}^2 + L_1M_{34}^2 - L_1L_3L_4 - 2M_{13}M_{14}M_{34}) \\ & + \omega^2(R_4M_{13}^2 + R_3M_{14}^2 + R_1M_{34}^2 - L_1L_3R_4 - L_1L_4R_3 - L_3L_4R_1) \\ & + j\omega(L_1R_3R_4 + L_3R_1R_4 + L_4R_1R_3) \\ & + R_1R_3R_4 \Big] \\ & \Big/ \Big[\omega^2(M_{34}^2 - L_3L_4) + j\omega(L_3R_4 + L_4R_3) + R_3R_4 \Big] \ [\Omega], \end{aligned} \tag{2.22}$$

$$
\begin{aligned}
Z_{22} = \Big[& j\omega^3(L_4M_{23}^2 + L_3M_{24}^2 + L_2M_{34}^2 - M_{23}M_{24}M_{34} - L_2L_3L_4) \\
& + \omega^2(R_4M_{23}^2 + R_3M_{24}^2 + R_2M_{34}^2 - L_2L_3R_4 - L_2L_4R_3 - L_3L_4R_2) \\
& + j\omega(L_2R_3R_4 + L_3R_2R_4 + L_4R_2R_3) \\
& + R_2R_3R_4\Big] \\
& \Big/ \Big[\omega^2(M_{34}^2 - L_3L_4) + j\omega(L_3R_4 + L_4R_3) + R_3R_4\Big] \ [\Omega],
\end{aligned}
\tag{2.23}
$$

$$
\begin{aligned}
Z_{12} = Z_{21} = \Big[& j\omega^3(M_{12}M_{34}^2 - L_3L_4M_{12} + L_4M_{13}M_{23} \\
& + L_3M_{14}M_{24} - M_{13}M_{24}M_{34} - M_{14}M_{23}M_{34}) \\
& + \omega^2(M_{13}M_{23}R_4 + M_{14}M_{24}R_3 - L_4M_{12}R_3 - L_3M_{12}R_4) \\
& + j\omega M_{12}R_3R_4\Big] \\
& \Big/ \Big[\omega^2(M_{34}^2 - L_3L_4) + j\omega(L_3R_4 + L_4R_3) + R_3R_4\Big] \ [\Omega].
\end{aligned}
\tag{2.24}
$$

2.8 Efficiency

The power transfer efficiency of the channel is the ratio of the real (or active) output power in the receiving coil to the real input power in the transmitting coil:

$$
\frac{P_S}{P_P} = \frac{\mathrm{Re}(V_1 I_1^*)}{\mathrm{Re}(V_2 I_2^*)}, \tag{2.25}
$$

where P, V and I are the are the real power, complex voltage and complex current on the primary and secondary sides, respectively, and * is the complex conjugate operator. The efficiency of the channel is not merely a property of the channel, since is affected by circuit level parameters.

Using the basic FHA model described in Section 2.4, an equation for the transfer ratio can be derived as

$$
\begin{aligned}
\frac{P_S}{P_P} = & \ \omega^4 C_S^2 M_{12}^2 R_L \\
& \Big/ \Big[\omega^4(R_P C_S^2 L_S^2 + C_S^2 M_{12}^2 R_S + C_S^2 M_{12}^2 R_L) \\
& + \omega^2(R_P C_S^2 R_S^2 + 2R_P C_S^2 R_S R_L + R_P C_S^2 R_L^2 - 2R_P C_S L_S) \\
& + R_P\Big].
\end{aligned}
\tag{2.26}
$$

As can be seen, the efficiency of the channel is dependent on channel parameters, most importantly the coil resistances, as well as circuit parameters such as the load resistance and resonance capacitor on the receiving side. The efficiency of the channel is reduced as power is consumed in the resistive parts of the coils. An example of how the efficiency changes with frequency is seen in Figure 2.6, where

two cases are displayed: one where the coil resistances R_P and R_S have a constant resistance of $1\,\Omega$, and one where they are modeled by fitting a second degree polynomial function to data from measurements of the coil resistances taken with an LCR meter. In the latter case, the resistance increases with frequency due to skin effect, as is displayed in Figure 4.3 in the *Results* chapter.

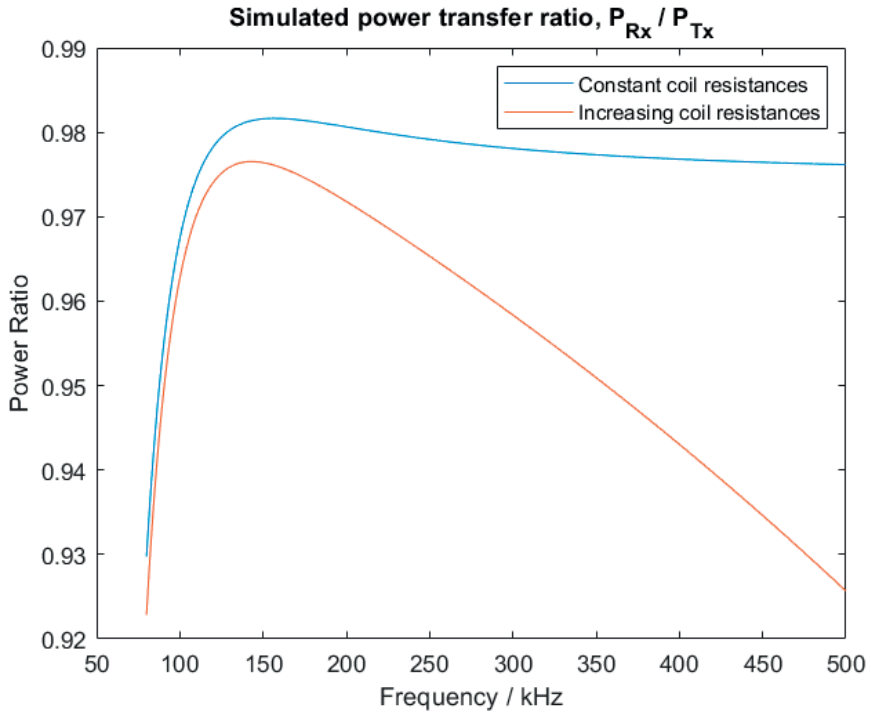

Figure 2.6: Efficiency of the system with constant coil resistances, as well as with coil resistances that are increasing with frequency due to skin effect.

Chapter 3
Methodology

This chapter describes how the project was carried out, focusing especially on the process that was used to obtain measurements.

An empirical approach was used to characterize the channel. The methodology was based on making measurements of the channel in various scenarios, and using the collected data to represent the channel as a two-port network via Z-parameters. The data was also used to obtain the power transfer efficiency for each scenario. In order to calculate Z-parameters, the magnitude and phase of voltages and currents on either coil are needed. To collect the necessary data, a custom measurement setup based on an oscilloscope was arranged, which was controlled by a PC running Matlab scripts.

3.1 Approach

It is possible to make Z-parameter measurements in a number of ways. The approach that is used in this thesis work is based on directly measuring voltages and currents, and their respective phases, using measurement devices (such as differential voltage probes) connected to an oscilloscope. Alternative methods include the use of a vector network analyzer (VNA) or an LCR meter. An LCR meter can measure the self inductances and mutual inductance of the system, as well as the resistances of either coils, but there does not seem to be a straightforward way to measure the mutual resistance, meaning that the real part of Z_{12} and Z_{21} are not captured with this method. Moreover, an issue that arises with both the LCR meter and the VNA is that the power that can be output from these devices is significantly lower (generally less than 1 W) than the operating power levels of WPT systems (up to 15 W in current Qi Specification devices). This limitation can be addressed by introducing a power amplifier (PA) to the system. However, the effect the PA has on the system has to be calibrated out in order for the characterization to be accurate, which requires additional equipment, adding significant complexity to the setup [14]. Further, including the PA puts the VNA and LCR meter at risk of being damaged, as these are sensitive devices that normally operate on low power.

Using an oscilloscope with measurement probes allows for currents and voltages to be measured directly over the transmitting and receiving coils, enabling the calculation of Z-parameters directly from these quantities.

3.2 Measurement Setup

A schematic of the measurement setup is given in Figure 3.1. In order for inductive power transfer to occur, a time varying current needs to be delivered to the primary coil. A sinusoidal signal is generated by a function generator and fed to a PA. The PA is connected in series to the primary (transmitting) coil and the resonance capacitor. The voltage signal generated by the function generator is amplified by a factor of 10, after which it drives a current through the primary coil. The voltage over the primary coil is measured by a differential voltage probe, and the current running through it is measured by a current measurement board. On the receiving side, the secondary (receiving) coil is connected in series to a resonance capacitor. Similarly to the transmitting side, the voltage over the secondary coil is measured using a differential voltage probe. The current is measured using a current measurement board, which leads the current to a connected resistive load.

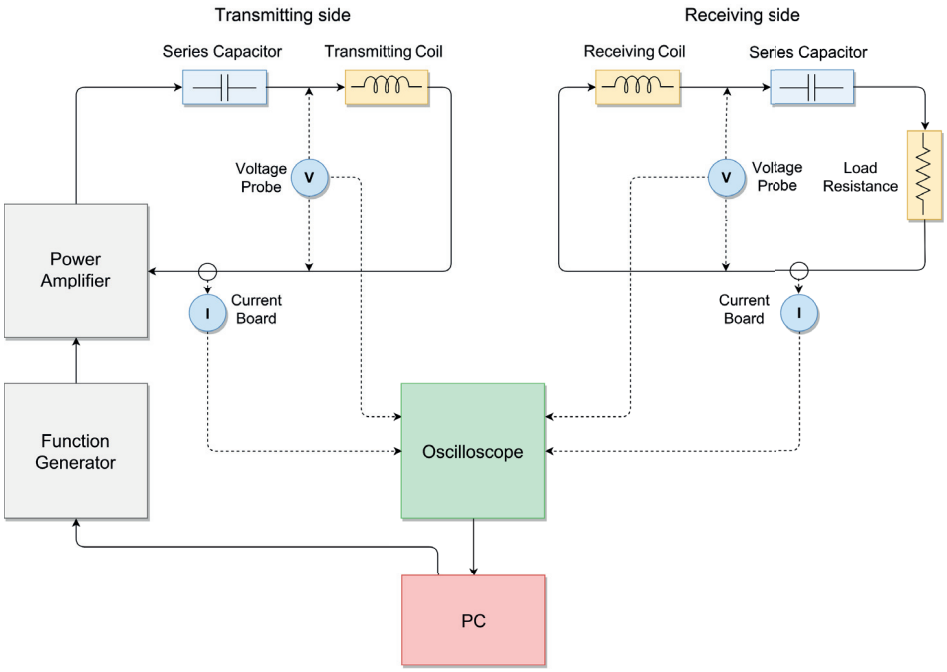

Figure 3.1: Schematic of the measurement setup.

3.3 Measurement Equipment

This section describes the equipment used for the channel measurements, which included:

- 33250A Function Generator - Agilent
- LPA05 Laboratory PA - N4L

- DPO3014 Digital Phosphor Oscilloscope - Tektronix
- AP031 Differential Probe - LeCroy
- P5200A High Voltage Differential Probe - Tektronix
- LCR-8101G LCR Meter - GW INSTEK
- Transmitting and receiving coils
- Current measurement boards
- Coil fixture
- Qi Specification representative FOs #1, #2 and #4.

3.3.1 Function Generator

The 33250A Function Generator was used to generate a sinusoidal voltage signal as input to the system. As the function generator is unable to generate large power outputs, a PA was needed. The function generator can be controlled from a PC, allowing for the input to be changed dynamically during measurements.

3.3.2 Power Amplifier

The PA used to deliver power to the system (i.e., LPA05 Laboratory Power Amplifier) has certain limits which in turn set limits regarding what frequencies and power levels can be targeted for measurement. The PA has a power output limit of 90 VA and a voltage input limit of 4 V peak-to-peak, making the maximum voltage output 40 V peak-to-peak. At high frequencies and power levels the PA distorts the signal, as described in Figure 3.2. This distortion becomes very apparent when the output voltage is close to 40 V and high frequencies are used.

3.3.3 Oscilloscopes

To calculate Z-parameters, voltages and currents need to be captured for both coils at the same time. Simultaneous capture allows for phase shifts between each pair of the quantities to be recorded. An oscilloscope with four analog input ports was chosen to do the measurements. Connected to the oscilloscope were two differential voltage probes as well as the outputs on the current measurement boards. Calibration was performed in order for the analog inputs to be scaled correctly. The calibration was done by measuring the voltage and current over a known resistance with a known voltage input and making sure the measured values match the expected ones by adjusting the scaling for each probe on the oscilloscope.

During the course of the project issues were found with the original oscilloscope (DPO3014), leading to different oscilloscopes being used (MDO3014 and MSO46). As data was analyzed, it was found that the real part of Z-parameters are very sensitive to measurement error, and require high accuracy equipment to be measured properly. Two of the relevant oscilloscope specifications are the number of bits used for analog to digital (A/D) conversion, as well as the DC gain

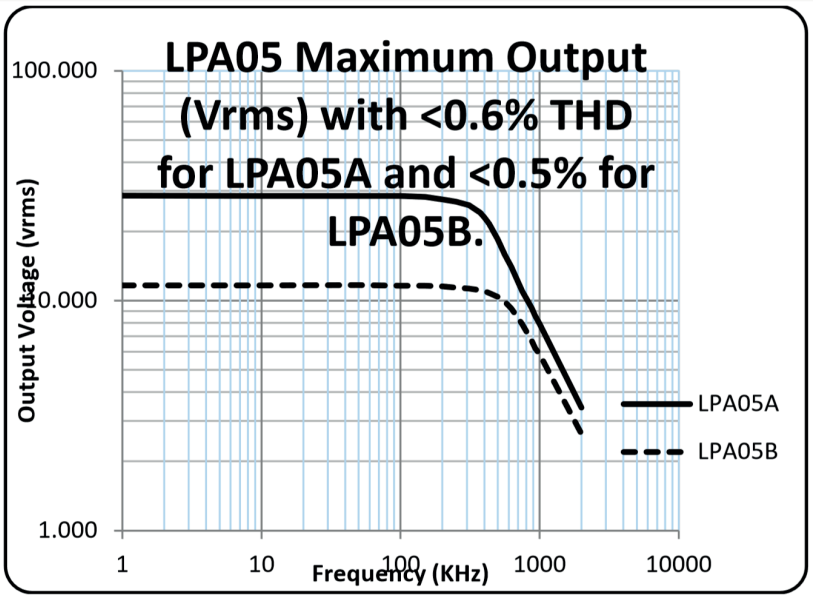

Figure 3.2: The dashed line shows the maximum voltage output for a total harmonic distortion of less than 0.5%, for the B version of LPA05, which was used in the measurement setup. The image is taken from the LPA05 user guide [15].

accuracy. The original oscilloscope (DPO3014) used 8 bits for A/D conversion with a gain accuracy ranging from $\pm 1.5\%$ to $\pm 2.5\%$ depending on the scaling set in the oscilloscope. The MSO3014 has the same vertical resolution and specified gain accuracy as the DPO3014, whereas the MSO46 has 12 bits for A/D conversion, with a vertical resolution of up to 16 bits using oversampling, and a DC gain accuracy of $\pm 1.0\%$ to $\pm 2.5\%$. The DPO3014 had issues causing significant changes in measured values to occur as vertical scaling was changed, likely due to different gain accuracies corresponding to different scaling.

3.3.4 Differential Voltage Probes

Two differential voltage probes were used to measure the voltage over the transmitting and receiving coils. For the transmitting coil, AP031 Differential Probe from LeCroy was used, and for the receiving coil, P5200A from Tektronix was used. These probes were used because they were available at the time and deemed sufficiently accurate for the purpose of the thesis work. Both probes report a gain accuracy of $\pm\,2\%$, which could be high enough to contribute to some of the issues that were seen in the measurement results, namely in the real part of Z-parameters, as small relative measurement errors can lead to large errors in the real part of Z-parameters, which will be discussed further in Section 4.2.2.

3.3.5 LCR meter

Coil parameters were measured using an LCR meter (LCR-8101G by GW Instek), which were used as a reference and a point of comparison. The LCR meter was used to measure the inductance and resistance of the transmitting and receiving coils, as well as the mutual inductance between them at different distances. The measurements were made at 100 kHz and 500 kHz, as this thesis focuses on the frequency range from 80-500 kHz, which will be discussed further in Section 3.5, *Measurement Scenarios*.

The mutual inductance between the coils can be calculated by measuring the equivalent inductance of the two coils when they are connected in series, such as they are aiding or opposing each other [16], as shown in Figure 3.3. When the coils are aiding each other, the inductance measured by the LCR meter is higher than that of either coil separately, whereas when the coils are opposing each other, the measured inductance is lower than that of either coil. One configuration can be obtained from the other, by switching the input and output connections on one of the coils. Using the measured inductances L_{aid} and L_{opp}, the mutual inductance can be calculated as:

$$M = \frac{L_{aid} - L_{opp}}{4} \ [\Omega]. \tag{3.1}$$

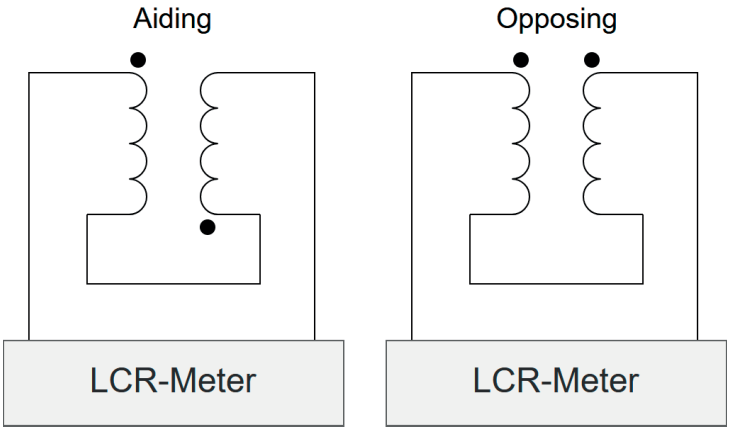

Figure 3.3: Coils connected in aiding and opposing configurations for measurement of mutual inductance.

3.3.6 Transmitting and Receiving Coils

The coils used for transmitting and receiving are of the same type, with close to identical characteristics. They are of model TDK 12F2-MA2 G and are manufactured by TDK Corporation. They have a spiral structure with dimensions and characteristics described in Table 3.1. Each coil has a layer of ferrite attached to it, as can be seen in a picture of one of the coils in Figure 3.4. The purpose of the ferrite is to improve the coupling between the coils, and the attached ferrite is of Ni-Zn type.

Inductance	$10.7\,\mu$H
Resistance @ 100 kHz	$100\,\text{m}\Omega$
Turns	12
Outer Diameter	46 mm
Inner Diameter	20 mm
Wire Diameter	1 mm
Layers	1
Ferrite Thickness	2.5 mm
Ferrite Side Length	52.0 mm
Ferrite Relative Permeability	800
Ferrite Resistivity	$> 10^5\,\Omega$m

Table 3.1: Coil dimensions and parameters.

3.3.7 Coil Fixture

A fixture was constructed with the purpose of keeping the transmitting and receiving coils at specific vertical and lateral separation distances during measurements. The fixture can be seen in Figures 3.5 and 3.6. Each coil is attached to one of two surfaces in the fixture; one which can be moved laterally by turning a dial; and one which can be moved vertically by inserting spacers. The lateral distance could be changed between 0 mm and around 35 mm. The vertical spacers that were used had a thickness of 1.5 mm, and the minimum distance from surface to surface between the coils being 1.3 mm (as limited by the thickness of the black plastic layer separating the two coil surfaces). The minimum vertical distance is achieved by putting the upper coil directly on the black plastic layer below it. The possible vertical distances between the coils were 1.3 mm as well as any multiple of 1.5 mm, which is the thickness of the vertical spacers, added to an initial distance of 2 mm. The initial distance is set by the upper coil being attached to the "default position" of the transparent plastic layer shown in Figure 3.5.

3.3.8 Foreign Objects

Foreign objects (FOs) are metallic objects that can be found near real power transfer situations and can have a negative impact on the WPT channel and the efficiency of power transfer. The Qi Specification devises test scenarios involving representative FOs, which are similar in size and characteristics to common household objects such as coins and key rings. The objects used in this investigation are Qi Specification's FOs #1, #2 and #4, which can be seen in Figure 3.7. Their respective size and shape can be found in Table 3.2. Additionally, thermal probes are incorporated in these objects to facilitate the thermal tests described in the Qi Specification.

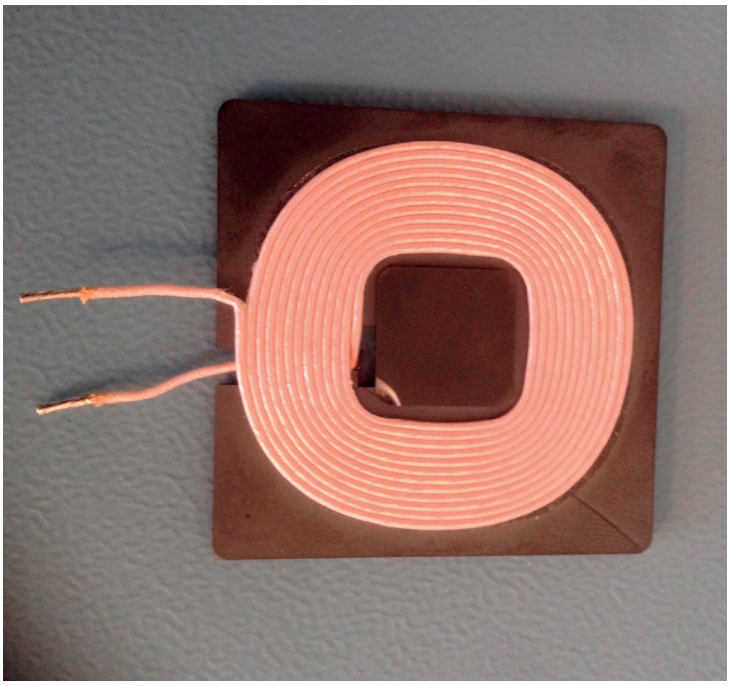

Figure 3.4: One of the identical coils used for power transfer.

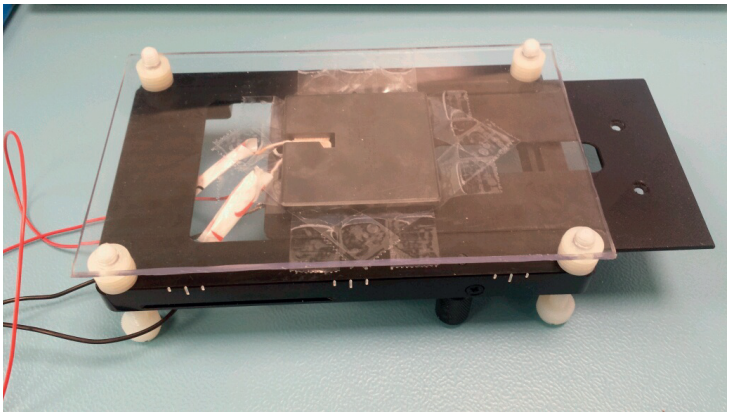

Figure 3.5: The fixture used to hold the coils and adjust distances (top side).

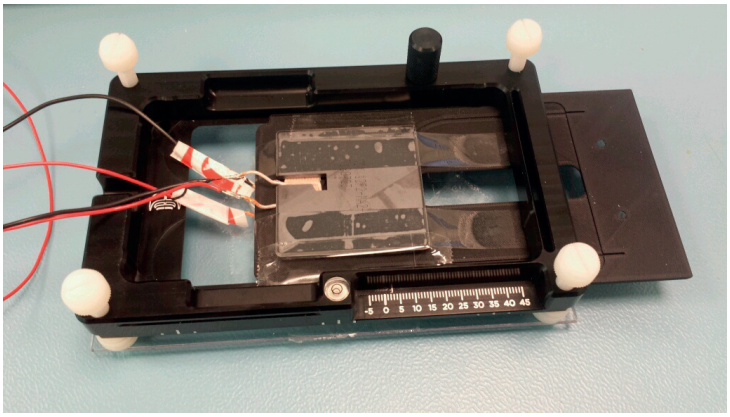

Figure 3.6: The fixture used to hold the coils and adjust distances (bottom side).

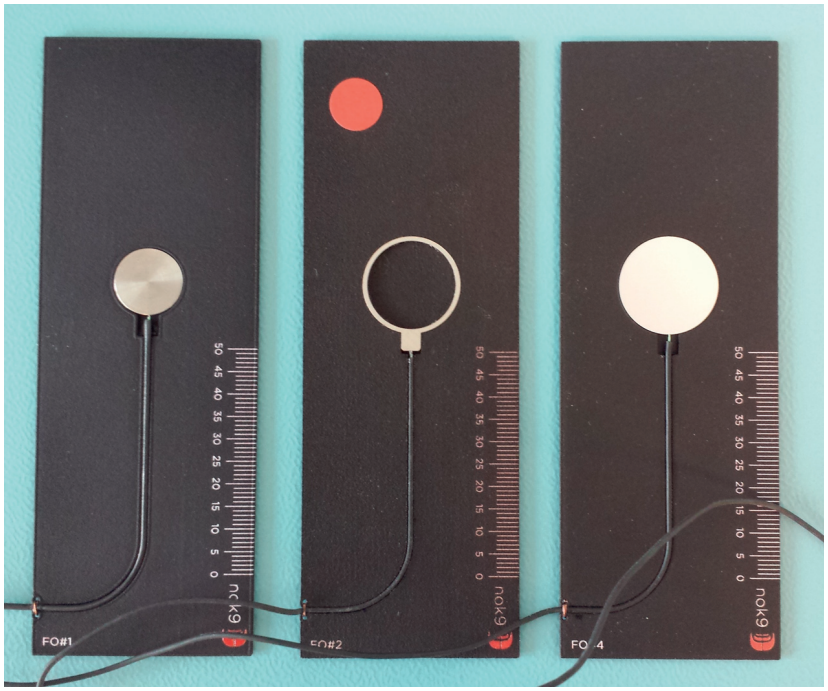

Figure 3.7: Photo of the FOs used. From left to right are FO #1, #2 and #4.

Object	Material	Shape	Diameter
#1	Steel	Disc	15 mm
#2	Aluminum	Ring	22 mm
#4	Aluminum	Disc	22 mm

Table 3.2: FO sizes.

3.4 Simulations

A program was developed in Matlab R2018b to make simulations based on the FHA model described in Section 2.4. The simulations allow for the calculations of currents, voltages and phase relationships using the FHA model. Knowledge how the voltage and current quantities relate to one another has been useful for finding values of system parameters for the measurement setup. Additionally the simulations were used as a reference for comparison with measurement data. Differences that have been found between measured and simulated results have triggered more detailed investigations, which have been useful both for gaining insights into underlying physical phenomenon, as well as for finding potential issues with the measurement equipment.

An example showing the result of a simulation of the current through a resistive load connected to the secondary side can be seen in Figure 3.8. The table next to the figure shows the simulation parameters.

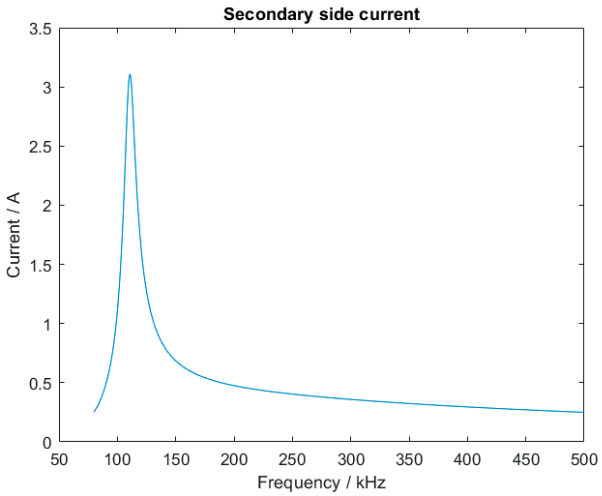

Parameter	Value
V_{IN}	10 V
L_P	15.4 μH
L_S	15.3 μH
C_P	0.1 μF
C_S	0.1 μF
k	0.73
R_L	20 Ω

Figure 3.8: Simulated current through a resistive load, based on the basic FHA model.

3.5 Measurement Scenarios

Measurements were made in various measurement scenarios at different operating points. The scenarios were defined based on what might be relevant in realistically

occurring charging situations, as well as on what might give interesting results. The different scenarios were defined by the variations of the following parameters:

- **Frequency:** Measurements were made in the frequency range of 80 kHz to 500 kHz. From 80 kHz to 150 kHz measurements were made every 2.5 kHz. In the range from 150 kHz to 500 kHz measurements were made every 17.5 kHz, giving a total of 49 frequency points. The Qi Specification targets operation in the 87-205 kHz frequency range, and much attention is being directed to WPT applications with operating frequencies of up to 500 kHz. With this in mind, and because the resonant circuits used in this thesis are tuned to have a resonance frequency close to 100 kHz, with the effective impedances becoming larger further away from the resonance frequency, 80 kHz and 500 kHz were was chosen as the lower and upper frequency limits of this investigation.
- **Levels of Power:** The power levels being targeted were 1 W, 3.5 W, 5 W 7.5 W, 10 W, 14.5 W and 15 W. Because of hardware limitations, data could not be collected for the higher powers for every operating scenario. Frequencies far from resonance, as well as low coupling factor, require large input voltages in order to reach the higher power, beyond the 40 V limit of the PA.
- **Coil Distance:** The vertical and lateral distance between the coils were varied using the coil fixture. The following tables shows the vertical and lateral distances used with their corresponding coupling factors. For each lateral distance, the vertical distance of 2 mm is used. The vertical distance is measured from surface to surface between the coils, and the lateral distance from center to center, as illustrated in Figure 3.9.

Vertical Distance	k
1.3 mm	0.89
2.0 mm	0.78
3.5 mm	0.73
5.0 mm	0.65
6.5 mm	0.57
8.0 mm	0.50

Lateral Distance	k
0 mm	0.78
4.0 mm	0.82
8.0 mm	0.70
12.0 mm	0.52
14.0 mm	0.43

The coupling factors shown were calculated from measurements of self inductances and mutual inductance taken with an LCR meter.

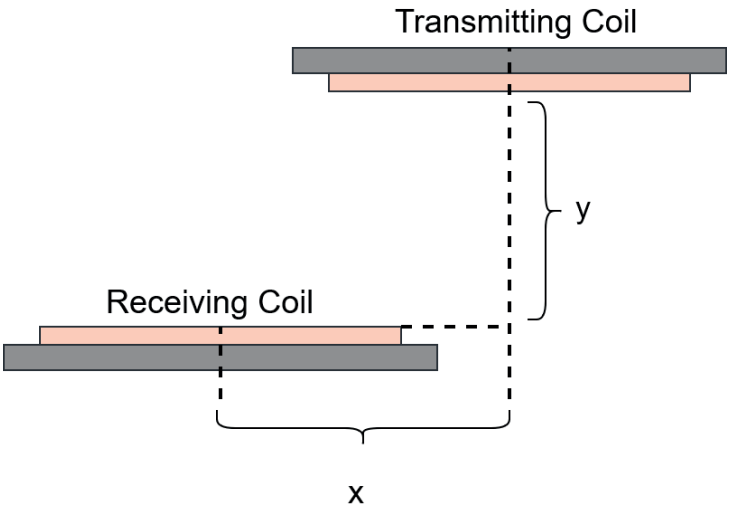

Figure 3.9: Illustration of coil separation, where y is the vertical, surface to surface separation distance, and x is the lateral, center to center separation distance.

- **Load Resistance:** Measurements were made using loads with resistances of 10 Ω, 13 Ω and 20 Ω. Measurements taken with two different loads were needed in order to calculate Z-parameters. The 10 Ω and 20 Ω loads were used in all Z-parameter measurements, with the exception of the FO measurements, where the 10 Ω and 13 Ω loads were used. The 13 Ω load was used instead of the 20 Ω load to minimize measurement error, as having two more similar loads requires a smaller change in the vertical scaling of the oscilloscopes, and variations in scaling can lead to variations in gain accuracy.

- **Foreign Objects:** FOs were put in the center between the transmitting and receiving coils during the measurements, as depicted in Figure 3.10. The objects that were used are Qi Specification representative FOs #1, #2 and #4.

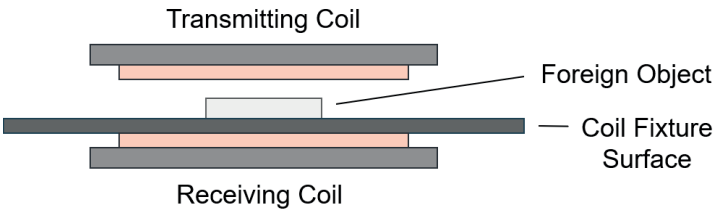

Figure 3.10: Illustration of placement of a FO.

3.6 Measurement Process

In the interest of streamlining data collection, the measurement process was automated to some extent. To achieve this, a custom software was developed in Matlab. The software was made to control the 33250A function generator as well as the Tektronix oscilloscopes. For a given set of frequencies, the software would ramp up the voltage at the coil system input until a target power level was reached. Once reached, the oscilloscope would make a measurement and the data would be saved. The voltage would then be further increased until all targeted power levels were reached, after which the process would be repeated for the next frequency point. Figure 3.11 shows how the voltage is ramped up for one frequency point.

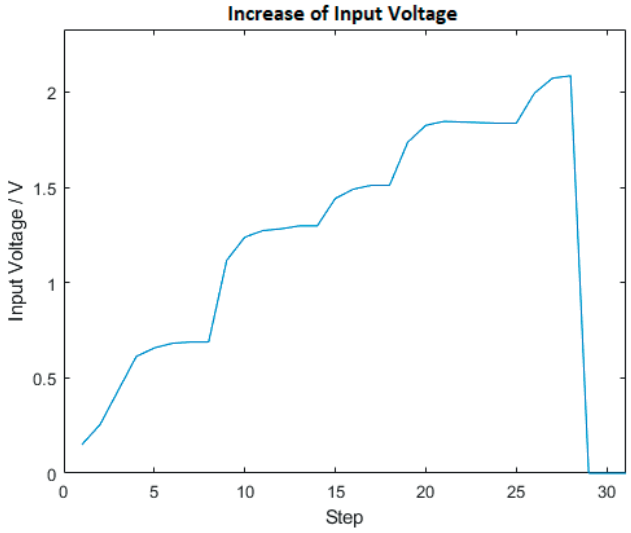

Figure 3.11: The voltage output from the function generator as it ramps up to reach various power levels.

Each measurement made by the oscilloscope would result in a waveform capture, consisting of a collection of data points showing the magnitude of each measured quantity over a number of cycles. The result from a frequency sweep would be a set of waveform captures, one for each measured quantity and power level, over the target range of frequencies. The main drawback of taking measurement at constant power levels is that the process is relatively time consuming, as the voltage needs to be increased in steps in order for the desired power level to be "found". A full measurement sweep including the full range of frequencies and power levels could take up to 40 minutes. For measurements made with FOs, a constant voltage was used, rather than constant power, both because the temperatures of the object became an issue, and in the interest of saving time.

In between frequency sweeps, one parameter of the setup would be manually changed, such as the adjustment of the distance between the coils, or the adding or removal of FOs.

3.7 Data Analysis

The data collected from the oscilloscope consisted of data points representing the magnitude of a voltage or current in the transmitting or receiving coils. A sine wave was fitted to the captured data points, resulting in data in the form of

$$A\sin(2\pi f \cdot t + \phi), \tag{3.2}$$

where A, f and ϕ are the resulting values, corresponding to amplitude, frequency and phase respectively. The phase can be considered arbitrary on its own, but it allows for phase differences to be calculated since the currents and voltages in each coil is measured simultaneously. The currents and voltages were represented as complex numbers, with the voltage over the primary coil being chosen as the reference phase quantity, with it being defined as having no imaginary part.

From the complex voltages and currents, Z-parameters can be calculated by rearranging (2.17). Four equations are needed for the four unknown Z-parameters, meaning that two sets of voltages and currents are necessary. The Z-parameters are calculated according to (3.3), (3.4), (3.5) and (3.6):

$$Z_{11} = \frac{V_1 - Z_{12}I_2}{I_1} \ [\Omega], \tag{3.3}$$

$$Z_{22} = \frac{V_2 - Z_{21}I_1}{I_2} \ [\Omega], \tag{3.4}$$

$$Z_{12} = \frac{V_{12}I_{11} - V_{11}I_{12}}{I_{11}I_{22} - I_{21}I_{12}} \ [\Omega], \tag{3.5}$$

$$Z_{21} = \frac{V_{22}I_{21} - V_{21}I_{22}}{I_{12}I_{21} - I_{11}I_{22}} \ [\Omega]. \tag{3.6}$$

In the equations for Z_{12} and Z_{21}, V_{mn} is the voltage over coil m (primary or secondary), from measurement set n. Measurements taken using two different loads provided the two measurement sets. At first, data from two different power levels were used to calculate the Z-parameters, however this proved unsuccessful as changing power has no effect on the relationship between voltages and currents (the observed small differences were due to experimental tolerances), and thus it does not provide independent equations. According to (2.6), (2.7), (2.8) and (2.9), both voltages and currents scale linearly with input voltage. For the voltages V_1 and V_2, this can be made clear by substituting (2.8) and (2.9) into (2.6) and (2.7):

$$V_1 = V_{IN}\frac{j\omega L_P Z_2 + \omega^2 M^2 + R_P Z_2}{Z_1 Z_2 + \omega^2 M^2} \ [\mathrm{V}], \tag{3.7}$$

$$V_2 = V_{IN}\frac{j\omega M Z_2 + \omega^2 L_S M - R_S M}{Z_1 Z_2 + \omega^2 M^2} \ [\mathrm{V}]. \tag{3.8}$$

Thus, using some input voltage V_{IN} for the first measurement set, and a scaled input voltage αV_{IN} for the second measurement set, where α is some scaling factor, means that $V_{m2} = \alpha V_{m1}$ and $I_{m2} = \alpha I_{m1}$. Substituting this into (3.5) and (3.6) gives:

$$Z_{12} = \frac{V_{12}I_{11} - V_{11}I_{12}}{I_{11}I_{22} - I_{21}I_{12}} = \frac{\alpha V_{11}I_{11} - V_{11}\alpha I_{11}}{I_{11}\alpha I_{21} - I_{21}\alpha I_{11}} = \frac{0}{0} \ [\Omega], \tag{3.9}$$

$$Z_{21} = \frac{V_{22}I_{21} - V_{21}I_{22}}{I_{12}I_{21} - I_{11}I_{22}} = \frac{\alpha V_{21}I_{21} - V_{21}\alpha I_{21}}{\alpha I_{11}I_{21} - I_{11}\alpha I_{21}} = \frac{0}{0} \ [\Omega]. \tag{3.10}$$

Both Z_{12} and Z_{21} are thus undefined. Using different loads for the two measurement sets works, as the voltages and currents scale differently with load resistance.

The power transfer efficiency of the channel was also calculated as the ratio of the real power in the receiving and transmitting coils, as described earlier in Section 2.8.

Chapter 4
Results

This chapter provides the results obtained from the voltage and current measurements taken with the procedure described in the previous chapter. Specifically, the results include real and imaginary parts of Z-parameters, as well as power transfer efficiency (or ratio), of the two-coil system for different scenarios of interest. The scenarios include different lateral and vertical separation distances between the coils, and the absence or presence of different FOs between the coils. In addition, some reference results obtained using an LCR meter are presented at the beginning of the chapter for later comparison and validation.

4.1 Reference LCR-measurements

Using the procedure described in Section 3.3.5, measurements of coil parameters were taken at various distances between the coils using an LCR meter. These parameters are presented in Table 4.1 and Table 4.2, and corresponding Figure 4.1 and Figure 4.2, which show the inductances and resistances respectively, and in which y denotes the vertical distance between the coil surfaces. The measurements were taken at 100 kHz and 500 kHz and 0.5 V input voltage.

The primary coil series resistance was also measured over a range of frequencies, displayed in Figure 4.3, illustrating the increase in resistance due to skin effect.

y	L_P	L_S	M	k
1.3 mm	21.8 μH	21.8 μH	19.4 μH	0.89
2.0 mm	18.2 μH	18.4 μH	14.3 μH	0.78
3.5 mm	15.3 μH	15.4 μH	11.3 μH	0.73
5.0 mm	13.8 μH	14.0 μH	9.1 μH	0.65
6.5 mm	12.8 μH	12.9 μH	7.3 μH	0.57
8.0 mm	12.2 μH	12.3 μH	6.1 μH	0.50

Table 4.1: Inductances and coupling factors for various distances, as measured by LCR meter

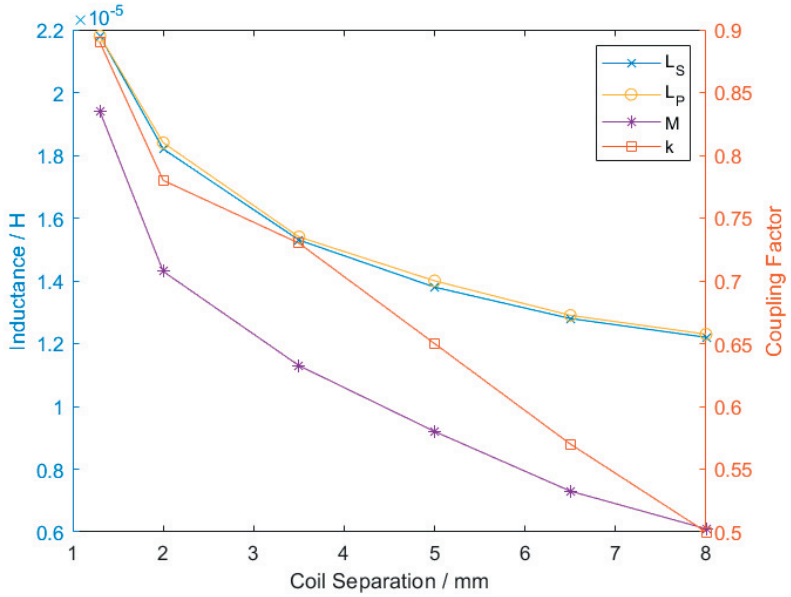

Figure 4.1: Inductances and coupling factor measured by LCR meter, for different vertical coil separations.

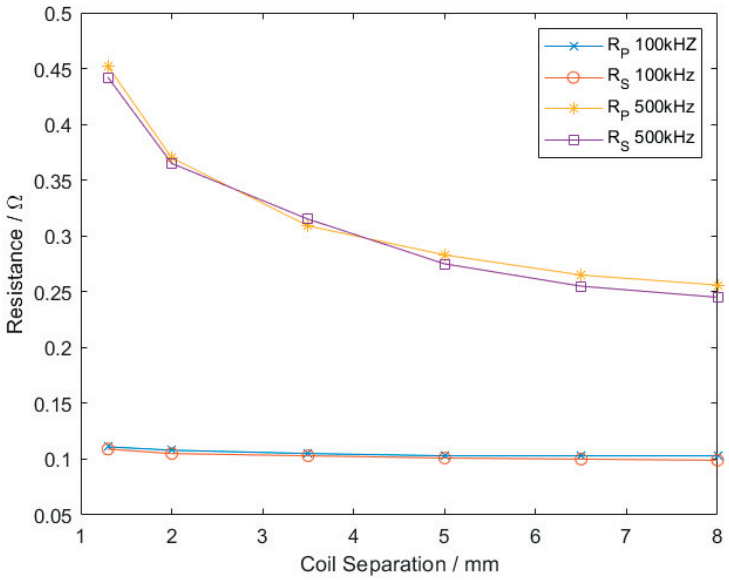

Figure 4.2: Resistances measured by LCR meter, for different vertical coil separations.

y	R_P 100 kHz	R_S 100 kHz	R_P 500 kHz	R_S 500 kHz
1.3 mm	111 mΩ	109 mΩ	452 mΩ	442 mΩ
2.0 mm	108 mΩ	105 mΩ	370 mΩ	365 mΩ
3.5 mm	105 mΩ	103 mΩ	309 mΩ	315 mΩ
5.0 mm	103 mΩ	101 mΩ	283 mΩ	275 mΩ
6.5 mm	103 mΩ	100 mΩ	265 mΩ	255 mΩ
8.0 mm	103 mΩ	99 mΩ	256 mΩ	245 mΩ

Table 4.2: Coil resistances for various distances, as measured by LCR meter

4.2 General Observations of Channel Measurements

As described in Chapter 3, to measure in-band communication channel subjected to realistic WPT operating conditions, the setup involving voltage and current measurements using a 4-channel oscilloscope was employed. Before detailed results are presented and discussed for the different scenarios, some general observations of the channel parameters, namely the real and imaginary parts of the channel in Z-parameter representation as well as power transfer efficiencies, are given. Particular attention is paid to unexpected behavior and corrective measures taken to improve the results.

4.2.1 Imaginary Part of Z-parameters

Z_{11} describes the contribution to the voltage over the primary coil from the current through it, whereas Z_{22} describes the same relationship but for the secondary coil. Z_{11} and Z_{22} have an imaginary part that was expected to be equal to the reactance resulting from the self inductance of either coil.

Z_{12} and Z_{21} were expected to be equal to each other due to reciprocity. They describe the contribution to the voltage on one side due to the current on the other side, and were initially expected only to have an imaginary part. Their expected magnitude was the mutual inductance of the two-coil system M times the angular frequency ω.

The reactive parts of different Z-parameters can be seen to be linearly increasing with frequency in Figure 4.4. The plot shows the imaginary parts of the calculated Z-parameters (based on measured coil voltages and currents) in a case where both coils are well aligned and have a distance of 3.5 mm in between, with an input power of 1 W. A more inclined slope corresponds to a higher mutual inductance or self inductance, and average inductances can be calculated from the displayed data by assuming the theoretical linear relationship between the measured reactance and the mutual or self inductance according to $X = j\omega M$ or $X = j\omega L$. There is a slight difference between the measured reactances in Z_{12} and Z_{21}, which can likely be attributed to measurement error, an issue that will be explored further in the analysis of the real parts of the Z-parameters.

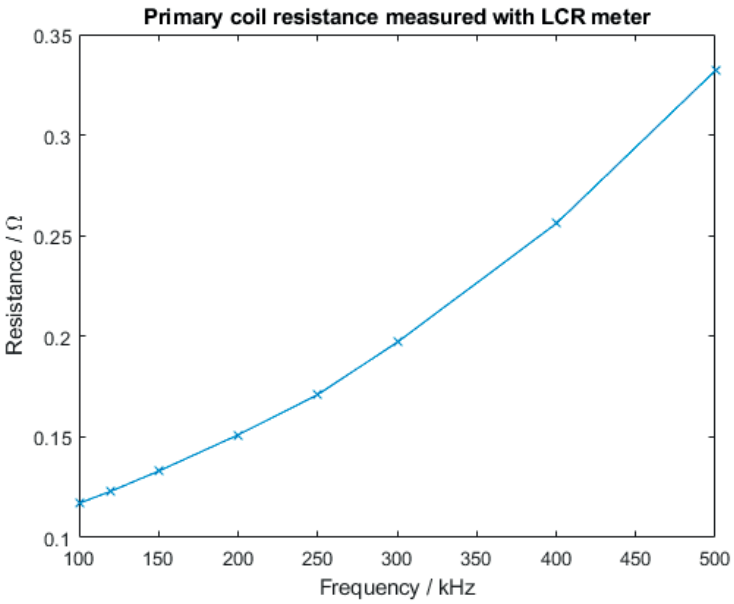

Figure 4.3: Primary coil series resistance, as measured by LCR meter.

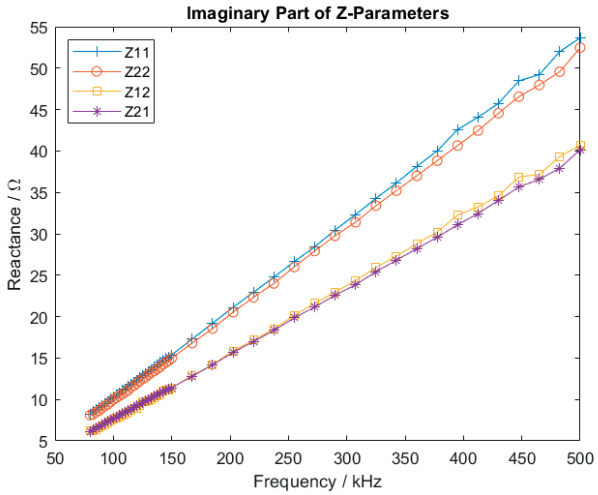

Parameter	Inductance
Z_{11}	16.6
Z_{22}	16.0
Z_{12}	12.3
Z_{21}	12.3

Figure 4.4: Imaginary parts of Z_{11}, Z_{12}, Z_{21} and Z_{22}, measured with input power of 1 W and at 3.5 mm vertical distance between the coils.

4.2.2 Real Part of Z-Parameters

Any non-zero real parts of the Z-parameters in the two port representation points to power loss in the channel. The main source of power loss was initially thought to be the inherent resistances in the wires that were formed into the coils. However, the measurement results suggest that additional sources of power loss can be found in the channel. Specifically, the real parts of Z_{12} and Z_{21} has been measured to be non-zero, when coil resistances can only be expected to affect Z_{11} and Z_{22}.

The real parts of the Z-parameters calculated from measurements were found to be noisy and highly sensitive to measurement error. The general trend seen in the real parts of the Z-parameters is that of increasing resistance with frequency, which is to be expected as skin effect causes resistance in wires to increase with frequency. One example of the real part of Z_{11} can be seen in Figure 4.5. Simulations based on the basic FHA model described in Section 2.4 shows that relatively small relative errors in the absolute values of some measured quantities (i.e., primary and secondary side current or voltage) translate to large relative errors in the real part of the Z-parameters. As an example, a simulation of the real part of Z_{11} can be seen in Figure 4.6, where a random error between 0 and $\pm 1\%$ of the total magnitude of each current and voltage over the primary and secondary coils has been added to the respective quantities for each frequency point. Figure 4.6 also shows the series resistance of the coil measured with the LCR meter for comparison. The added errors, despite being small in comparison to the total magnitude of the voltage and current quantities, lead to a large relative error in the real part of Z_{11}, which increases at higher frequencies.

The real parts of the Z-parameters represent a relatively small part of the absolute magnitude of the Z-parameters, as the real parts are generally on the scale of hundreds of milli-ohms, whereas the imaginary parts are on the scale of tens of ohms over the frequency range of interest, causing noise to be present to a high degree in the real parts, but not in the imaginary parts. Further, simulations suggest that the sensitivity to noise increases at higher frequencies, due to the linear increase in the imaginary part (reactance) with frequency making the real part becoming even smaller in proportion to the absolute value of the complex impedance. This causes the larger spikes that can be seen in Figure 4.5 and that are characteristic of the collected measurement data.

The real parts of Z_{12} and Z_{21} for a specific set of parameters are plotted in Figure 4.7. In a reciprocal system, Z_{12} and Z_{21} can be expected to be the same, as is the case for the FHA models described in Section 2.4 and Section 2.6. The differences seen in Figure 4.7 is likely connected to measurement error, as different measured quantities were used to calculate these parameters.

Using the basic FHA model described in Section 2.4, the real parts of Z_{12} and Z_{21} are both zero for any frequency, whereas in the extended model described in Section 2.6 there are frequency dependent terms in the real parts of Z_{12} and Z_{21}. This suggests that without nearby coils or objects which can consume power in the generated magnetic field, the real parts of Z_{12} and Z_{21} should remain zero, which is not the case in the measured parameters. A possible explanation for the non-zero real parts of Z_{12} and Z_{21} is that power is consumed in the ferrites attached to the transmitting and receiving coils, as the ferrites are the only objects

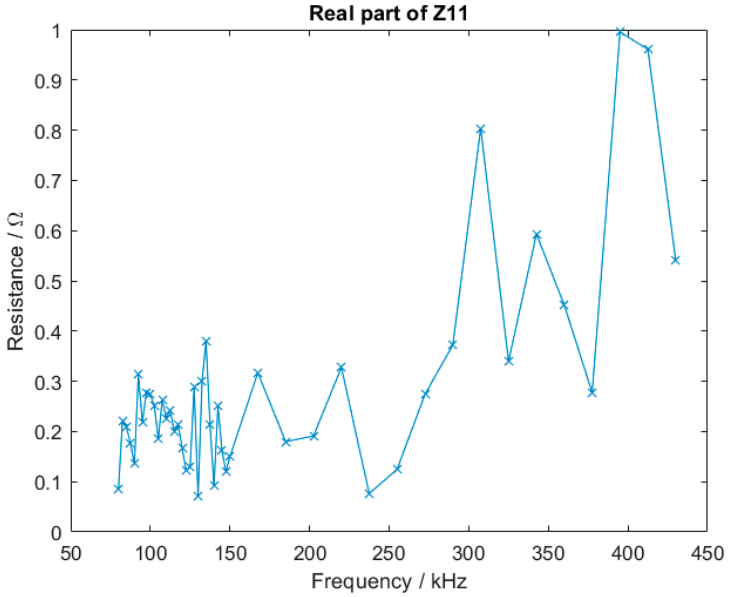

Figure 4.5: Real part of Z_{11}, measured with input power 3.5 W and at 3.5 mm vertical distance using MSO3014.

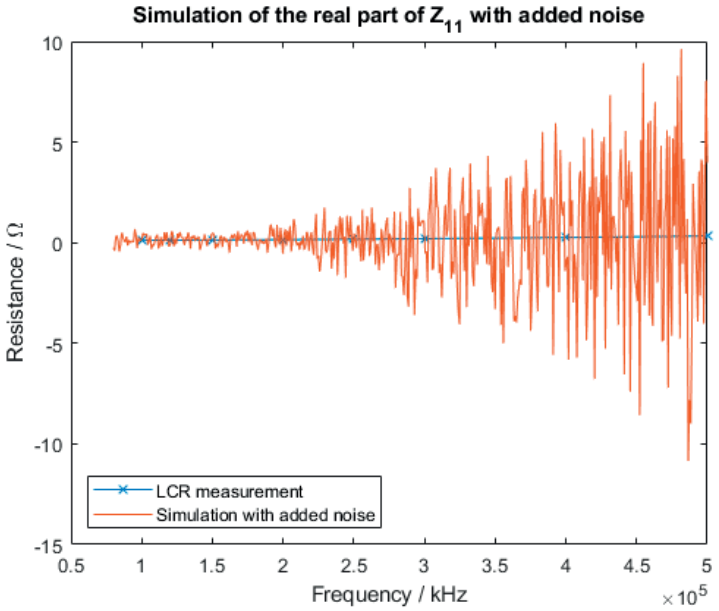

Figure 4.6: Real part of Z_{11} simulated with added noise, and measured with LCR meter.

in close proximity to the power transfer system with any real potential to support eddy currents. Taking the real parts of the expressions for Z_{12} and Z_{21} from the extended FHA model, we get:

$$\begin{aligned}\mathrm{Re}(Z_{12}) = \mathrm{Re}(Z_{21}) = \Big[&\omega^4\big(M_{13}M_{23}M_{34}^2R_4 + M_{14}M_{24}M_{34}^2R_3 \\ &- L_3M_{13}M_{24}M_{34}R_4 - L_3M_{14}M_{23}M_{34}R_4 - L_4M_{13}M_{24}M_{34}R_3 \\ &- L_4M_{14}M_{23}M_{34}R_3 + L_4^2M_{13}M_{23}R_3 + L_3^2M_{14}M_{24}R_4\big) \\ &+ \omega^2\big(M_{14}M_{24}R_3^2R_4 + M_{13}M_{23}R_3R_4^2\big)\Big] \\ \Big/\Big[&\omega^4\big(L_3^2L_4^2 - 2L_3L_4M_{34}^2 + M_{34}^4\big) \\ &+ \omega^2\big(L_3^2R_4^2 + L_4^2R_3^2 + 2M_{34}^2R_3R_4\big) + R_3^2R_4^2\Big] \ \ [\Omega],\end{aligned} \tag{4.1}$$

which shows resistance being highly frequency dependent. The high resistivity of the ferrite material should inhibit the formation of eddy currents, meaning the expected power loss in the ferrite sheets is very low, and hence this loss is unlikely to result in a contribution to the resistive parts of the Z-parameters exceeding the contribution of the inherent coil resistance, which is in many cases seen in the measurement results. Again, the general noisy nature and inconsistency in the real parts of the Z-parameters make it difficult to draw strong conclusions based on this aspect of the measurement results.

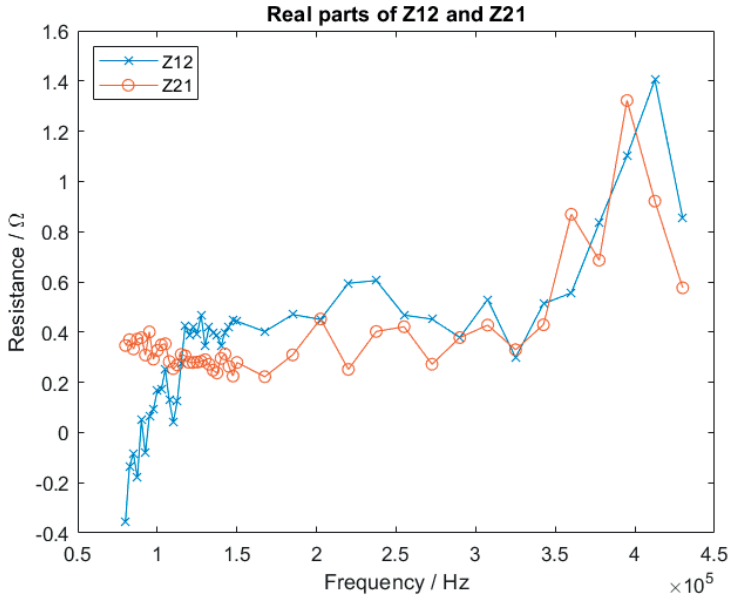

Figure 4.7: Real parts of Z_{12} and Z_{21}, measured with input power 3.5 W and at 3.5 mm vertical distance using MSO3014.

Some likely sources of measurement error can be found in the properties of

the oscilloscopes used, specifically the number of bits used for A/D conversion, as well as the DC gain accuracy. The vertical scaling used during a measurement decides how many volts or amperes correspond to each possible conversion level (i.e., quantization interval); ideally the full range of possible levels should be used to minimize quantization error. Using the oscilloscope DPO 3014, different trends could be observed in the measured Z-parameters depending on whether the vertical scaling used by the oscilloscope would be similar for both sets of measurements (using different loads) for some specific voltage or current. A mechanical change could be heard in the oscilloscope as scaling was changed above or below a certain voltage or current value. Significant changes in the real part of Z-parameters could be observed if one set of measurements was taken above and one was taken below this value, for some measured quantity. This can be observed in Figure 4.8, where significant jumps and changes in trend can be seen around 200 kHz and 250 kHz. It is reported in the oscilloscope data sheet that gain accuracy may change with vertical scaling.

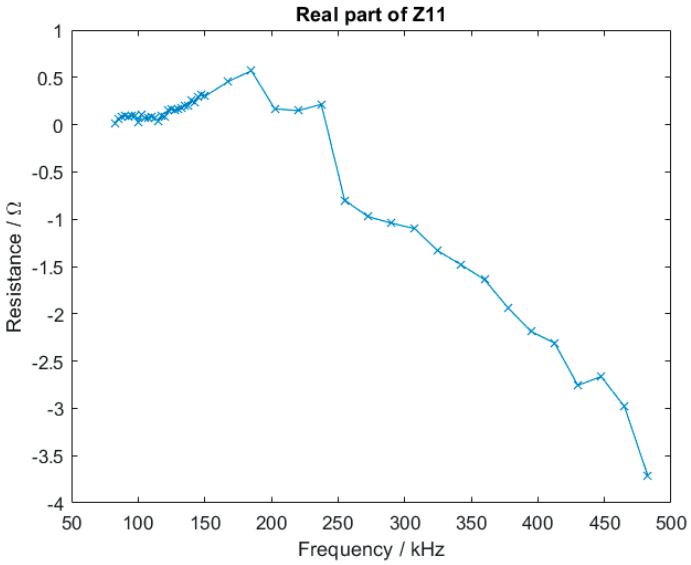

Figure 4.8: Real part of Z_{11}, measured with input power 3.5 W and at 3.5 mm vertical distance using DPO3014.

Changing the oscilloscope to MSO3014 improved the results as there was no sudden drastic change in trend, however, the noise remained. Further, an additional oscilloscope was used, the MSO46, which has up to 16 bits vertical resolution, providing significantly improved accuracy. Measurements made using the MSO46 shows much less noise, however, the measured real parts of Z-parameters has values which are not within the range that may be reasonably expected. Measurements of the real part of Z-parameters using MSO46 can be seen in Figure 4.9, which shows the resistance corresponding to Z_{11} reaching above 2.5 Ω at high frequencies, whereas Z_{22} takes on negative values, which makes little physical sense as it would imply that power is generated rather than consumed as currents travel

through the receiving coil. Measurements with the LCR meter show the resistance of the coils to be below 500 mΩ at 100 kHz and 500 kHz.

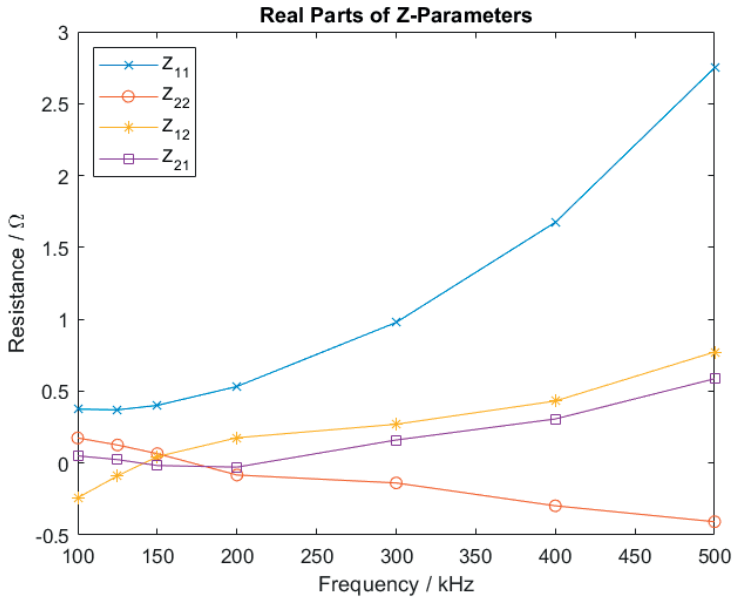

Figure 4.9: Real parts of Z-parameters, using an input voltage of 15 V, and a vertical coil separation of 3.5 mm, from measurements taken with the MSO46 oscilloscope.

Despite multiple attempts, a complete explanation of the peculiar behavior seen in the real part of Z-parameters is still elusive. Simulations using the basic FHA model show, however, that some relative error (e.g., 1%) present in one measured quantity (such as the voltage over the transmitting coil) in one data set (using one of the two different loads needed for two data sets) but not the other, gives simulation results with similar trends to the measured results. This can be seen in Figure 4.10, in which Z_{11} has been simulated based on the basic FHA model. In the simulation, the resistances of the primary and secondary coil have been fitted to the data from LCR meter measurement of the coil series resistance (shown in Figure 4.3), and a constant relative error of 1% has been added to the primary coil voltage. The simulated resistance in Z_{11} with the added error has a large deviation from the case with no added error, with it taking even negative values and reaching a magnitude of more than ten times the case with no error. With the error added to the primary coil voltage, Z_{22} and Z_{12} are unaffected whereas Z_{11} and Z_{21} are affected, showing that the Z-parameters are affected differently by the errors added to different quantities. The Z-parameters measured using MSO46, shown in Figure 4.9, have behavior that could be explained this way. Quantization error from the oscilloscopes is very likely to differ for each data point, and as such can be expected to be different in the two data sets needed for Z-parameter calculation, giving rise to the noise that can be seen in measurements taken with the 8-bit oscilloscopes. On the other hand, MSO46 has

very little quantization error, and as such there is very little noise in the real part of the Z-parameters, as opposed to the trend seen in Figure 4.5. Nonetheless, its results in Figure 4.9 remain problematic. These observations seem to suggest that a systematic error (or bias) in the measurement of a voltage or current quantity (rather than quantization error) may be responsible for the unexpected results seen in Figure 4.9.

Further, simulations where the same relative error is present in both measurement sets do not give the large deviations shown in Figure 4.10. It is thus important when measuring the Z-parameters to make sure that the measurement conditions do not change between measurement sets. As the magnitude of voltages and currents change between measurement sets due to the load changing, small offset errors, or changes in gain accuracy due to changes in vertical resolution could provide enough relative error to be highly noticeable in the results. As such, it is possible there is such systematic error(s) in the measurement setup. One possible source of error, other than the oscilloscopes, is the differential voltage probes used for measurement, as they have a reported gain accuracy of $\pm 2\%$, which could contribute to the unexpected results.

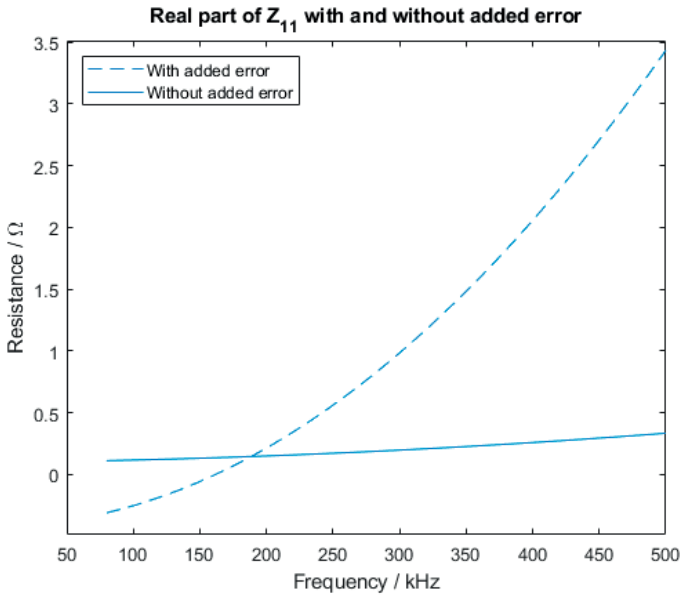

Figure 4.10: Real part of Z_{11} with and without error added to the primary coil voltage, obtained from simulations.

4.2.3 Power Transfer Efficiency

Power can be calculated from the voltage across- and current through a coil. With good coupling, the calculated power in the receiving coil is expected to be similar to that of the transmitting coil (but with reversed sign, as the receiving coil appears to be generating power, whereas the transmitting coil appears to consume power),

since the power that is seen going out from the receiving coil must also be seen going in to the transmitting coil. With ideal coils, the ratio of the received to transmitted power should remain 1, granted that there is no nearby object picking up some amount of the transmitted power. Realistically, both coils will have some amount of internal resistances, causing power to be lost to heating as the current travels through it. For this reason the power transfer efficiency will always remain below 1.

The reduction in power transfer efficiency from 1 happens largely due to the power loss in the resistive parts of the transmitting and receiving coils. However, the power ratio is also dependent on the circuit elements outside the coil-to-coil channel, such as the load resistor and the resonance capacitors, since these external elements influence the equivalent resistances as seen into the coil terminals. Figure 4.11 shows the power ratio for one case. Simulation result based on the basic FHA model (using similar parameter values) is also displayed, with the expression used for the simulated power ratio being (2.26), and the coil resistances used in the simulation being values from the measurements with the LCR meter. Interestingly, the peak efficiency does not occur at the resonance frequency, but instead it occurs at a slightly higher frequency. Resonance frequency for either side is calculated to be around 100 kHz, around which the currents peak, whereas the simulated peak transfer occurs at around 150 kHz. This is not surprising, since the coupling factor was measured by LCR meter to be 0.73 for this scenario, according to Table 4.1, so the presence of the secondary circuit loads the primary circuit and modifies its resonance behavior (and vice-versa). Moreover, it should be noted that maximum transfer ratio does not mean that maximum power is delivered to the load for some set voltage input, rather it only implies minimum percentage of power loss in the transfer.

4.3 Impact of Varying Input Power

Measurements have been done at different levels of power input to the transmitting coil, ranging from 1 W to 15 W. No significant impact from varying power input in the WPT channel has been observed in the Z-parameters. Differences in the measured results from using different input powers would indicate non-linearity in the system, something that can potentially be caused by non-linear components, e.g., the ferrite layers. However, with the measurement sensitivity that was available, no such non-linearity was seen in the Z-parameters. Nevertheless, the efficiency of the WPT system can be seen in Figure 4.13 to decrease slightly with increased input power.

A possible explanation for the decreased efficiency is that the increased power causes heating in the coils, which can increase their resistance, and thus reduce efficiency. The power that goes into heating the primary and secondary coils is given by $P = I_1^2 R_P + I_2^2 R_S$, and the exact temperature reached by the coils depends on the specific heat of the coil material, the structure and layout of the coil, and the surrounding temperature. The increase in resistance in a conductor due to changes in temperature is mostly linear, and can be approximated by

$$R = R_{ref}\big[1 + \alpha(T - T_{ref})\big] \ \ [\Omega], \tag{4.2}$$

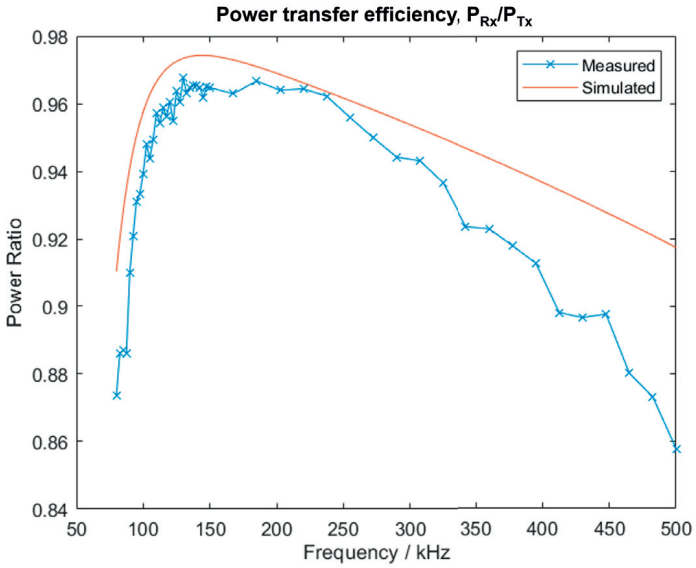

Figure 4.11: Power transfer efficiency for one scenario with 3.5 mm vertical distance between coils, and 1 W power in the transmitting coil, which a load resistance of 10 Ω. Measured and simulated results are displayed.

where T is the material temperature, T_{ref} is the temperature at which the material has some reference resistance R_{ref}, and α is the temperature coefficient for the material, which is 0.004041 for copper (at 20°). A temperature increase of a few degrees would thus lead to an increase in resistance in the order of tens of milliohms, which can explain the observed decrease in efficiency, as the coil resistance has been measured to be between 110 mΩ and 350 mΩ depending on the frequency for low power (less than 1 W).

4.4 Impact of Varying Distance

4.4.1 Imaginary Parts of Z-parameters

Changing the distance between the coils was found to affect both the mutual inductance and the self inductance of either coil. Figures 4.15 and 4.14 show the measured reactance corresponding to Z_{11} and Z_{12} for various distances. The average mutual inductance and self inductance can be calculated from the Z-parameters, and these values are displayed alongside the plots.

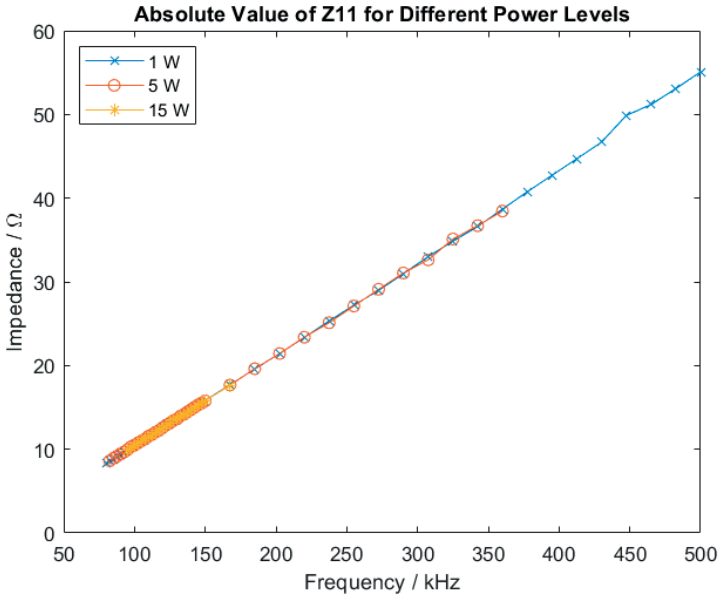

Figure 4.12: Absolute value of Z_{11} for different levels of power, using a vertical coil separation of 3.5 mm.

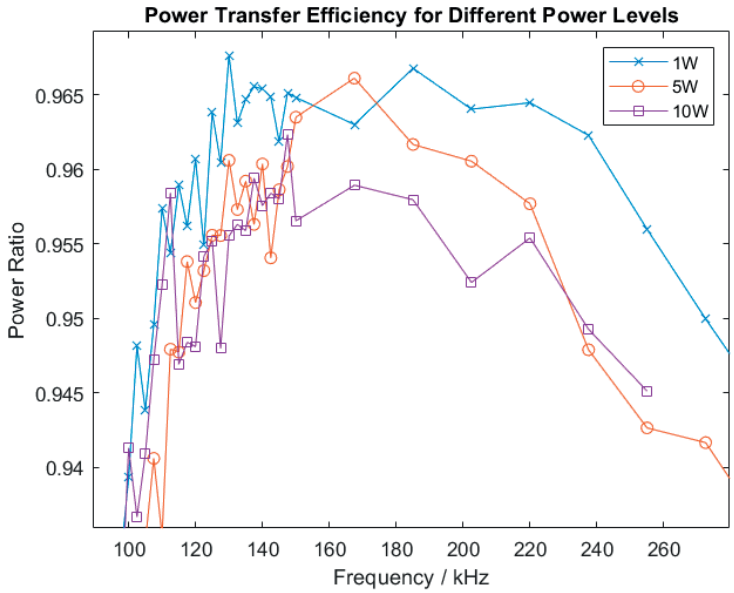

Figure 4.13: Power transfer efficiency for different power inputs, with 3.5 mm vertical distance between the coils, and a load resistance of 10 Ω.

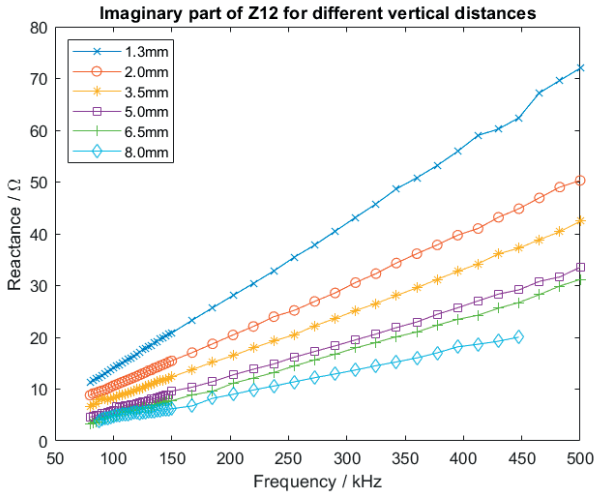

y	M
1.3 mm	22.3 μH
2.0 mm	16.4 μH
3.5 mm	13.2 μH
5.0 mm	9.8 μH
6.5 mm	8.4 μH
8.0 mm	7.1 μH

Figure 4.14: Imaginary part of Z_{12} for different vertical distances between coils.

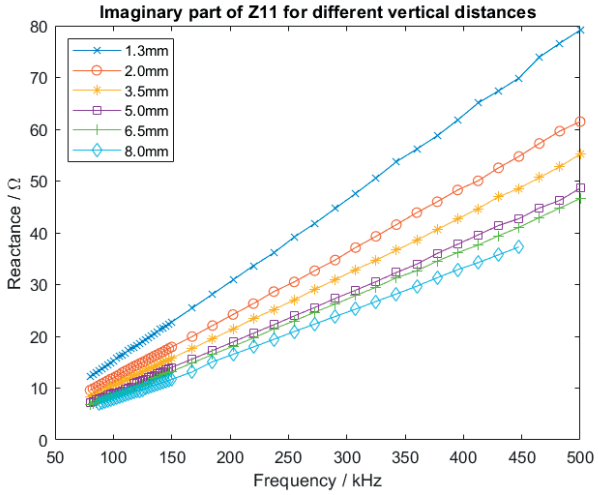

y	L_P
1.3 mm	24.4 μH
2.0 mm	19.2 μH
3.5 mm	16.8 μH
5.0 mm	14.7 μH
6.5 mm	14.0 μH
8.0 mm	12.7 μH

Figure 4.15: Imaginary part of Z_{11} for different vertical distances between coils.

The mutual inductance increases as the distance between the coils decreases, as seen in Figure 4.14. Not only the mutual inductance increases with decreased distance, but also the self inductances of either coil, as can be seen for the primary coil in Figure 4.15. This shows that the self inductance is not merely a property of the coil, but is also affected by the ferrites in the system. When one coil is moved closer to the other coil, the distance between the coil and the layer of ferrite attached to the opposite coil is also decreased, which causes an increase in self inductance. Because of the ferrites' effect on the coil inductances, the relationship between coil separation distance and self/mutual inductance becomes difficult to quantify.

y	L_P	L_S	M_{12}	M_{21}	M_{avg}	k
1.3 mm	24.4 μH	24.4 μH	22.3 μH	21.8 μH	22.1 μH	0.90
2.0 mm	19.2 μH	19.1 μH	16.4 μH	15.6 μH	16.0 μH	0.84
3.5 mm	16.8 μH	16.8 μH	13.2 μH	12.8 μH	13.0 μH	0.77
5.0 mm	14.7 μH	14.3 μH	9.8 μH	9.8 μH	9.8 μH	0.68
6.5 mm	14.0 μH	13.5 μH	8.4 μH	8.5 μH	8.4 μH	0.61
8.0 mm	12.7 μH	12.7 μH	7.1 μH	6.6 μH	6.9 μH	0.54

Table 4.3: Inductances and coupling factor calculated from Z-parameters, for vertical coil separation with distance y. M_{avg} is the average of M_{12} and M_{21}.

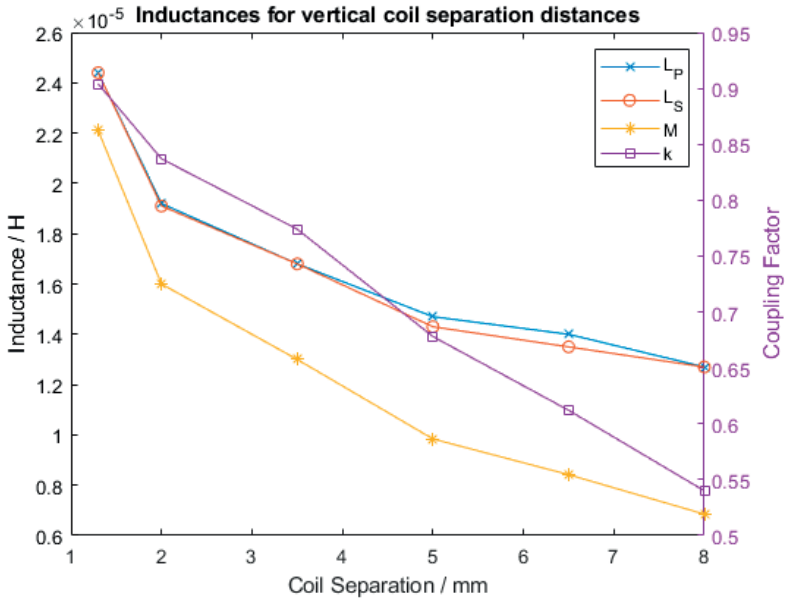

Figure 4.16: Calculated inductances for different vertical coil separation distances. M is the average of M_{12} and M_{21} and it corresponds to M_{avg} in Table 4.3.

Table 4.3 shows the inductances calculated from the Z-parameters, for various vertical distances y, and for a power input of 1 W. The inductances and coupling factors are all higher than the corresponding values obtained from measurements made with the LCR meter. The inductances are between 2% and 12% higher than the same inductances measured by the LCR meter. The accuracy in the measurement equipment, i.e. the gain accuracy in the oscilloscope and probes, may have contributed to this discrepancy. As the measurements were taken at different times, coil positioning is likely also a cause of discrepancy. For example, if the coils are slightly further apart during the measurement made with the LCR meter, it would cause a decrease in the measured self inductance.

Changing the lateral positioning of the coils has a similar effect on the Z-parameters to changing the vertical distance. The imaginary part of Z_{12} can be seen in Figure 4.17, in which x denotes the lateral offset between the center of the coils. The calculated self inductances for either coil, the mutual inductance, and the coupling factor for different lateral coil separation distances can be seen in Table 4.4 and Figure 4.18. The self inductances can be seen to be increasing as the offset between the coils is increased, until they reach a peak and start to decrease.

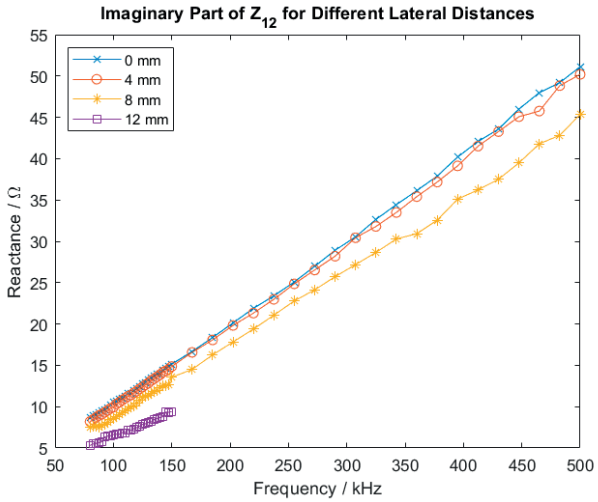

x	M
0 mm	16.4 μH
4.0 mm	15.8 μH
8.0 mm	14.0 μH
12.0 mm	10.2 μH

Figure 4.17: Imaginary part of Z_{12} for various lateral distances, using an input power of 1 W, and a vertical distance of 2.0 mm.

4.4.2 Real Parts of Z-Parameters

The measurements made using the LCR meter, displayed in Table 4.2, shows the resistances of the coils increasing as the coils get closer to each other. This is especially noticeable at higher frequencies. The same trend can be seen in the real parts of Z_{11} and Z_{22} for higher frequencies. Figure 4.19 shows the real part of Z_{11}, in which the resistance increases with increased distance for lower frequencies, and decreasing with increased distance for higher frequencies.

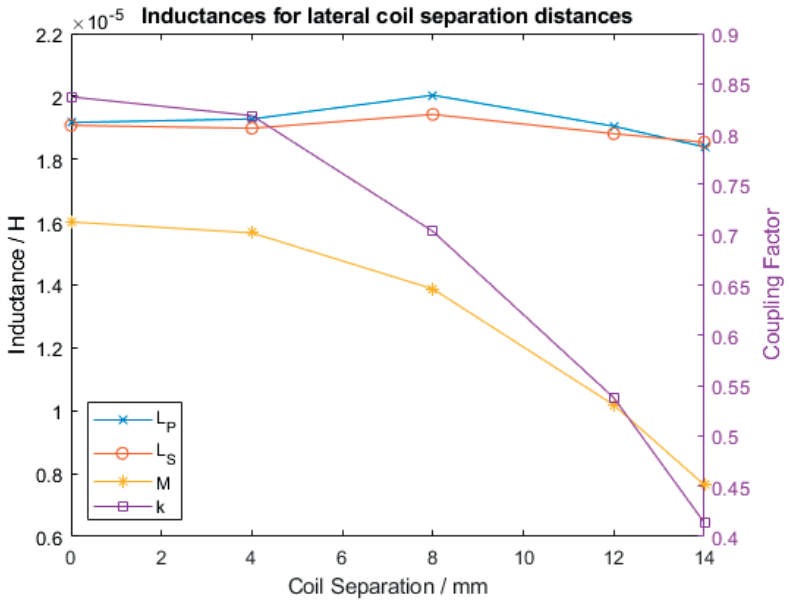

Figure 4.18: Calculated inductances for different lateral coil separation distances. M is the average of M_{12} and M_{21} and it corresponds to M_{avg} in Table 4.4.

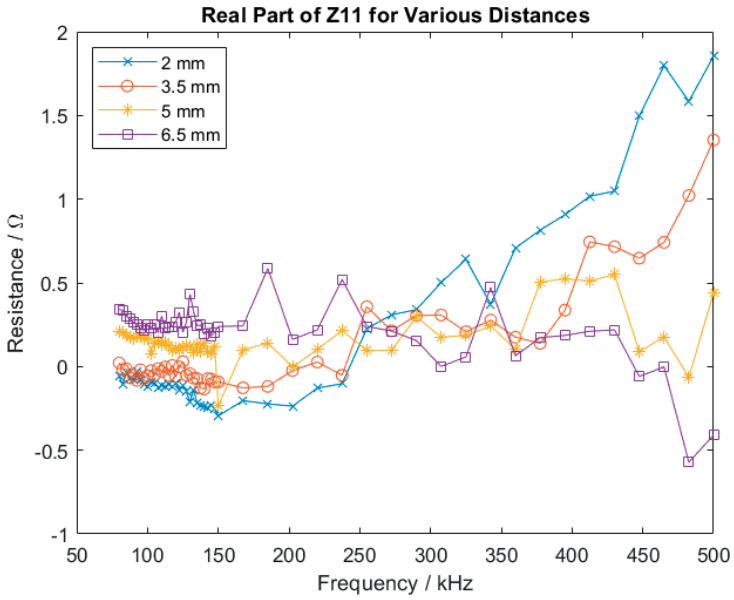

Figure 4.19: Real part of Z_{11} for various vertical distances, using an input power of 1 W.

x	L_P	L_S	M_{12}	M_{21}	M_{avg}	k
0 mm	19.2 μH	19.1 μH	16.4 μH	15.6 μH	16.0 μH	0.84
4.0 mm	19.3 μH	19.0 μH	15.8 μH	15.5 μH	15.7 μH	0.82
8.0 mm	20.0 μH	19.4 μH	14.0 μH	13.8 μH	13.9 μH	0.70
12.0 mm	19.1 μH	18.8 μH	10.2 μH	10.2 μH	10.2 μH	0.54
14.0 mm	18.4 μH	18.5 μH	7.6 μH	7.7 μH	7.6 μH	0.41

Table 4.4: Inductances and coupling factor calculated from Z-parameters, for lateral coil separation with distance x. M_{avg} is the average of M_{12} and M_{21}.

4.4.3 Power Transfer Efficiency

Increasing the distance between the coils has the effect of reducing power transfer efficiency, as can be observed in Figure 4.20. Both the maximum efficiency and the rate at which the efficiency is decreased with increasing frequency is increased. The decreased mutual inductance, lowered due to the increased distance between the coils, as well as the increased distance between coils and ferrites, leads to a decrease in efficiency, as can also be seen in (2.26). Further, although not entirely clear from Figure 4.20, the frequency of peak efficiency has been observed to change with distance, shifting toward higher frequencies with increased coil-to-coil distance. This can be made clearer by smoothing the curve using smoothing splines, as shown in Figure 4.21.

4.5 Impact of Foreign Objects

Transferring power in the presence of a metallic object can have a significant impact on the transfer system. In this investigation, Qi reference FOs #1, #2 and #4, described in Section 3.3.8, were placed in between the transmitting and receiving coils (one at a time), aligned laterally in the center between the coils. The measurements were taken using the MSO46 oscilloscope, with a constant voltage input of 15 V, and a vertical distance of 3.5 mm between the coils, with the FO directly in the middle. For the two measurement sets required for the calculation of the Z-parameters, load resistances of 10 Ω and 13 Ω were used.

4.5.1 Imaginary Part of Z-Parameters

The impact of the FOs on the mutual- and self reactance of the WPT system can be seen in Figures 4.23 and 4.24, with the corresponding tables providing the average inductance values. There is a significant decrease in both mutual- and self inductance when a FO is present, with FO#4, the aluminum disc, having the largest impact.

Similarly to the suggested use of coils to model eddy currents in ferrites, the same FHA model can be used to model eddy currents in FOs. Using one of the additional coils in the expanded FHA model to represent a FO, and removing

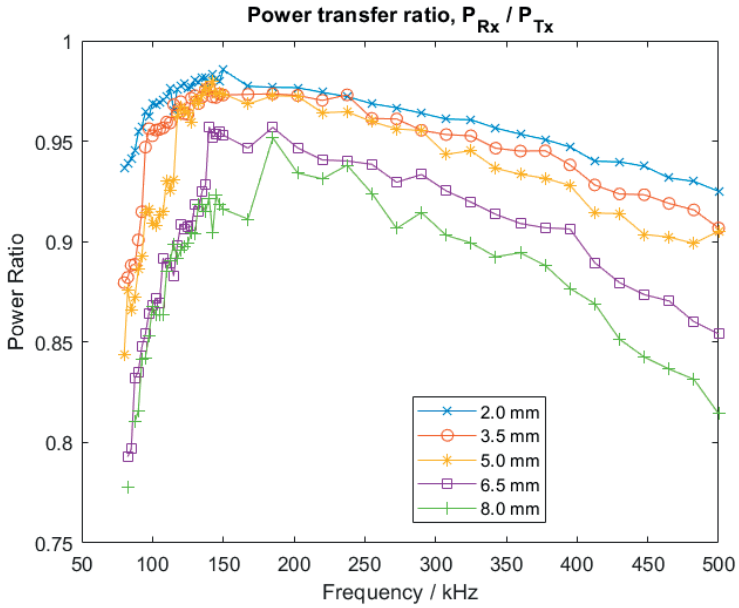

Figure 4.20: The power transfer efficiency for various vertical distances, using a power input of 1 W, and a load resistance of 10 Ω.

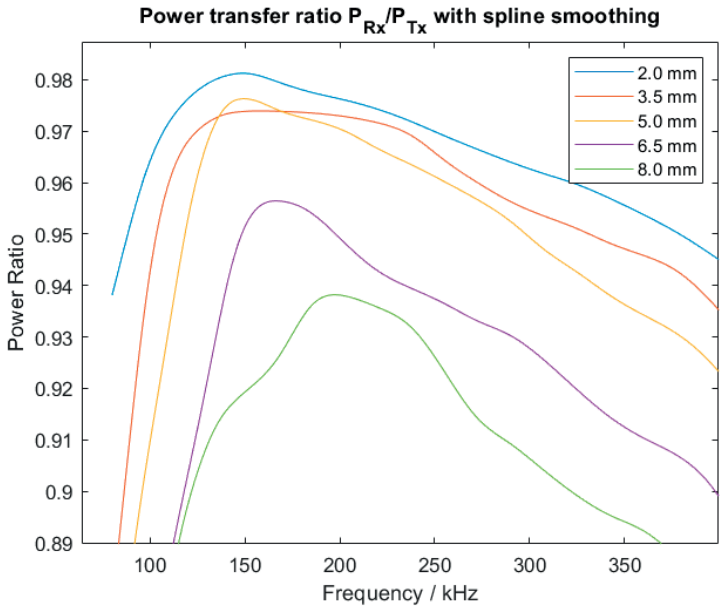

Figure 4.21: The power transfer efficiency for various vertical distances using smoothing splines, using a power input of 1 W, and a load resistance of 10 Ω.

the second additional coil as depicted in Figure 4.22, the expressions for the Z-parameters in Section 2.7, equations (2.22), (2.23) and (2.24), can be examined to gain an idea of how a FO may impact the Z-parameters. Taking the imaginary part, and setting M_{m4} to 0, gives the following expressions:

$$\mathrm{Im}(Z_{11}) = \omega L_P - \frac{\omega^3 L_3 M_{13}^2}{\omega^2 L_3^2 + R_3^2} \ [\Omega], \tag{4.3}$$

$$\mathrm{Im}(Z_{22}) = \omega L_S - \frac{\omega^3 L_3 M_{12}^2}{\omega^2 L_3^2 + R_3^2} \ [\Omega], \tag{4.4}$$

$$\mathrm{Im}(Z_{12}) = \omega M_{12} - \frac{\omega^3 L_3 M_{13} M_{23}}{\omega^2 L_3^2 + R_3^2} \ [\Omega]. \tag{4.5}$$

In these equations, it can be seen that the inductances are decreased with increased coupling to the additional coil representing the FO, as well as with decreased resistance of the object. High resistivity in materials impedes the formation of eddy currents, hence decreasing their impact on inductances.

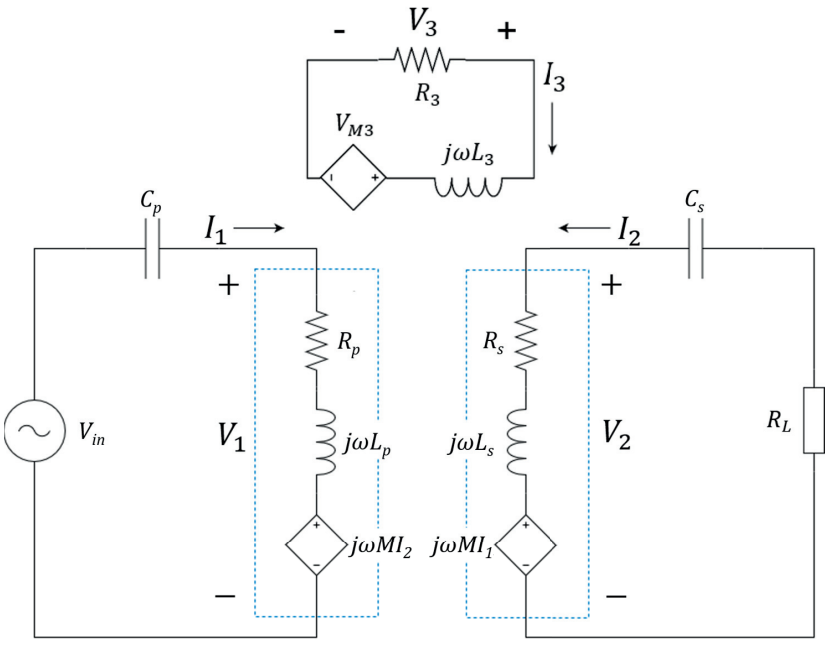

Figure 4.22: FHA model with an additional coil used to model eddy currents in a FO.

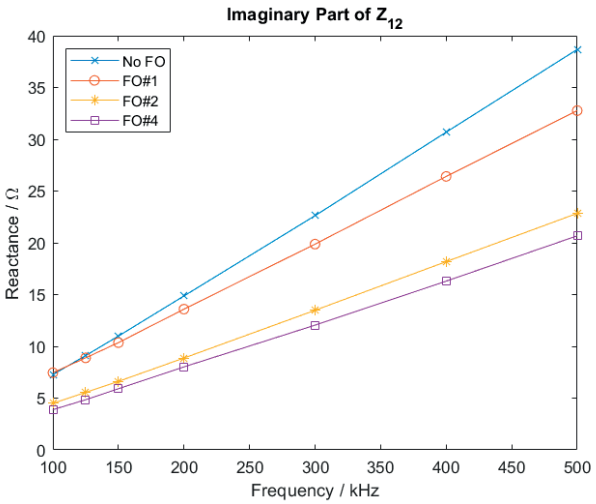

Object	M_{12}
Not present	11.9 μH
FO#1	10.9 μH
FO#2	7.14 μH
FO#4	6.35 μH

Figure 4.23: Imaginary part of Z_{12} with different FOs present.

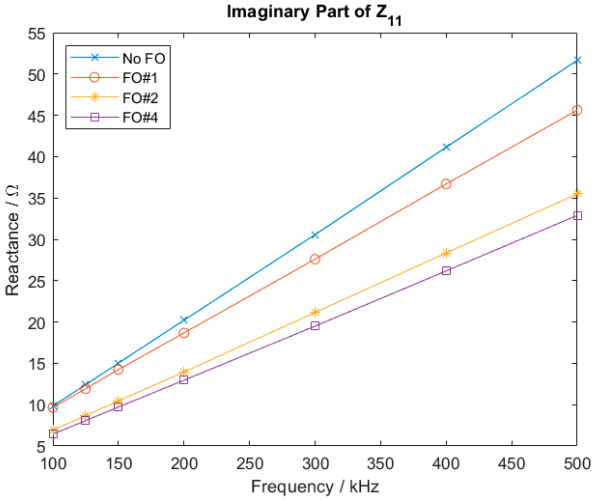

Object	L_P
Not present	16.1 μH
FO#1	14.9 μH
FO#2	11.2 μH
FO#4	10.3 μH

Figure 4.24: Imaginary part of Z_{11} with different FOs present.

4.5.2 Real Part of Z-parameters

The real part of the Z-parameters Z_{12} and Z_{11} can be seen in Figures 4.25 and 4.26. The resistances, which were measured using the MSO46, using load resistances of 10 Ω and 13 Ω, are for both parameters considerably high, both in cases with and without FOs. The real part of Z_{11} can be expected to be close to that of the inherent resistance in the primary coil, measured with LCR meter to be below 0.5 Ω for the 100-500 kHz range, whereas the Z-parameter measurements show a resistance of around 2.75 Ω at 500 kHz, which is much higher than what can be

expected, as measurements made with the LCR meter shows a significantly lower value, as seen in Table 4.2.

Although the uncertainty in the accuracy of the real parts of the Z-parameters makes it difficult to draw strong conclusions, nevertheless, from a relative standpoint, the observation shows the presence of FOs increases the resistance in Z_{12} (compared to no FO), as power is lost in the transfer between the coils. FO#1, the steel disc, which has the lowest impact on the imaginary parts, has the most significant impact on the real parts. Figure 4.26 shows that the resistance in Z_{11} is decreased when FO#2 and FO#4 is introduced at higher frequencies (from 200 kHz for FO #4 and 300 kHz for FO#2). This result is counter intuitive, since eddy currents in the FOs should add to the resistance as seen by the transmitting coil.

Similarly to the case of the imaginary parts of the Z-parameters, the expressions for the Z-parameters in Section 2.7 from the extended FHA model, modified to include only one additional coil, can be studied with respect to the real parts:

$$\mathrm{Re}(Z_{11}) = R_1 + \frac{\omega^2 M_{13}^2 R_3}{\omega^2 L_3^2 + R_3^2} \ [\Omega], \tag{4.6}$$

$$\mathrm{Re}(Z_{22}) = R_2 + \frac{\omega^2 M_{23}^2 R_3}{\omega^2 L_3^2 + R_3^2} \ [\Omega], \tag{4.7}$$

$$\mathrm{Re}(Z_{12}) = \frac{\omega^2 M_{13} M_{23} R_3}{\omega^2 L_3^2 + R_3^2} \ [\Omega]. \tag{4.8}$$

The expressions show that resistance is increased with higher coupling to the FO.

4.5.3 Power Transfer Ratio

The efficiency of the system is impacted negatively by the FOs as can be seen in Figure 4.27. This is because the power consumed in the object directly affects the efficiency of the system (less percentage of the power is transferred to the receiving coil). Decreasing the mutual inductance between the transmitting and receiving coils also has the contributes to the decreased power efficiency, similarly to when distance between the coils is increased, as discussed in Section 4.4.3. Interestingly, the frequency of peak power transfer efficiency can be observed to shift to higher frequencies with the presence of FOs. This is due to the reflected impedance from the FO changing the loading conditions as seen from the input terminals of the transmitting coils. The imaginary parts of Z_{11} and Z_{22} are reduced, effectively reducing the series inductance of the primary and secondary sides, and thus increasing the resonance frequency f_r according to (2.5).

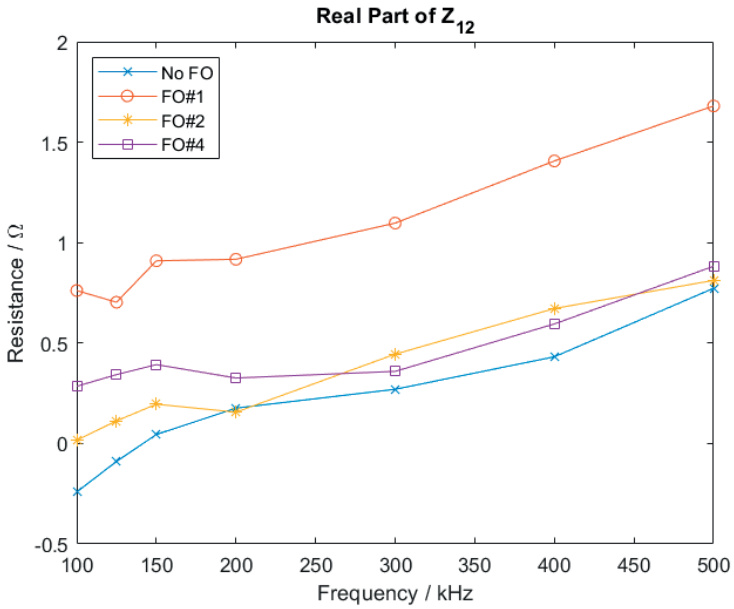

Figure 4.25: Real part of Z_{12} with different FOs present.

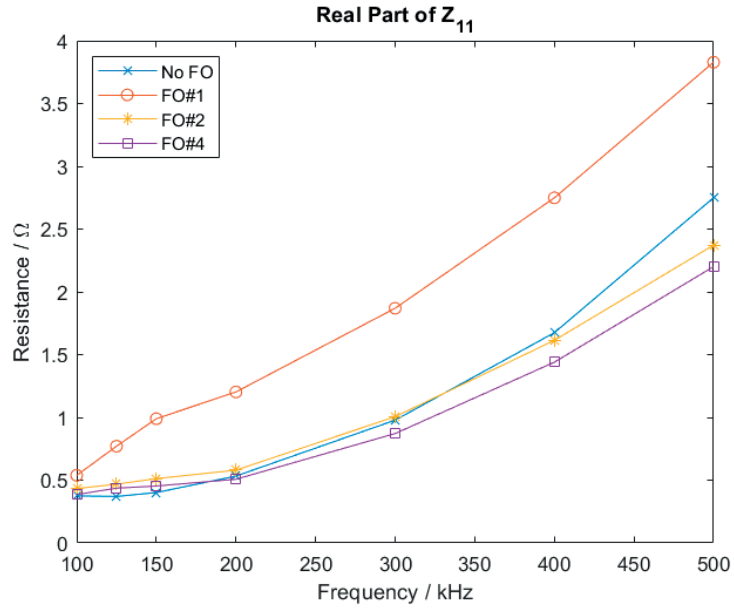

Figure 4.26: Real part of Z_{11} with different FOs present.

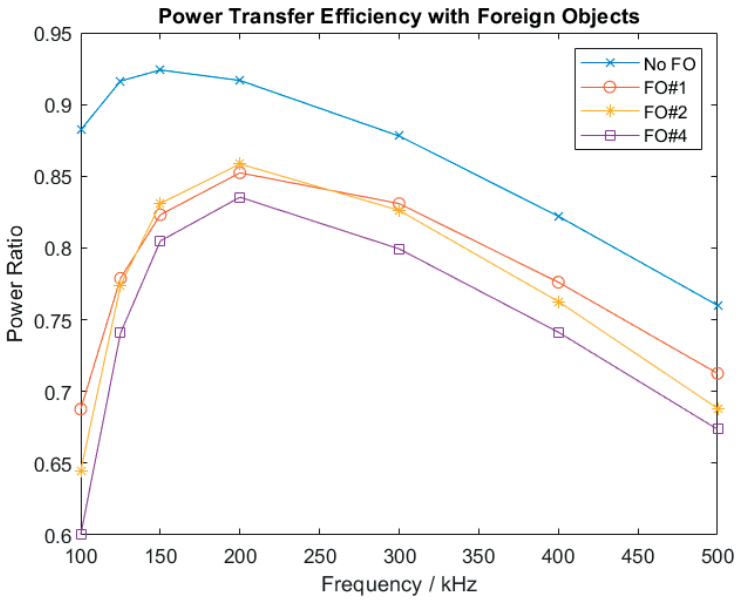

Figure 4.27: Power transfer efficiency of the WPT system with different FOs present.

Chapter 5

Conclusions and Future Work

5.1 Overall Conclusions

A measurement setup based around an oscilloscope has been made and used to measure the Z-parameters of the WPT coil-to-coil channel for various usage scenarios. The method has been validated for correctly extracting the Z-parameters of the channel. However, the accuracy of the measurements has been found to be lacking in certain regards, especially in obtaining the real parts of the Z-parameters. The analysis shows that this is at least in part due to the real parts of the Z-parameters (i.e., resistances) being significantly lower in magnitude than the imaginary part (i.e., the reactive counterpart). The resulting large dynamic range in the extracted parameters points to the requirement for highly accurate measurement instruments, including the oscilloscopes and the differential voltage probes. Simulations have shown that large errors can be present in the real parts of Z-parameters if there is a relatively small error in one of the two measurement sets needed for the Z-parameter calculation. It is thus highly important to keep measurement conditions and equipment accuracy consistent over different sets of measurement. Further tests using an oscilloscope with higher signal amplitude resolution (12-bit digitizer) resulted in reduced measurement noise. However, systematic errors were present in the measured quantities (which resulted in e.g., negative resistances) for some scenarios. This could be attributed to the accuracy problem in the voltage probes used. Due to time limitation, voltage probe calibration had not been investigated in detail.

Despite the accuracy issue, certain conclusions can still be made regarding the behavior of the channel in different scenarios. As can be expected, the self inductance of the coils as well as the mutual inductance have been shown to be affected significantly by the distance between the coils, as well as by the presence of foreign objects (FOs). The real parts of the Z-parameters have also been shown to change with the presence of FOs, and, interestingly, with distance between the coils, a phenomenon that could possibly be explained by varying power loss in the ferrite layers attached to the coils with coil separation distance. The collected data also reveal that, for the transmitter power (up to 15W) and frequency range (up to 500kHz) considered, the channel Z-parameters remain stable (from magnitude of impedance point of view), indicating the potential nonlinear components in the system (e.g., the ferrite layer attached to each coil) do not significantly affect the

linearity of the system under these operating conditions.

The power transfer efficiency of a WPT system is determined only in part by channel characteristics, most importantly the internal coils resistances. It has been observed to peak at frequencies higher than the resonance frequencies of the primary and secondary sides. Analysis of this phenomenon using an analytical model (FHA) showed that this behavior is tied to the reflected impedance on the primary side changing the load conditions as seen from the input terminals, modifying the resonance behavior. As the coupling of the coils changes (e.g., due to coil separation distance or presence of FOs), the frequency for peak efficiency can therefore shift.

Another important take away is that the basic FHA model can be used to make predictions of the WPT system. Simulation results obtained using this analytical model agree fairly well with the measured results. There are, however, some discrepancies, some of which can be attributed to eddy current losses. Therefore, the model has been extended to include two virtual coils to account for eddy current losses in the ferrite layers and the FOs. Although no attempt has been made to investigate in detail the new parameters of the extended model (for example, the resistance and self-inductance of the virtual coils), it was used to find expressions showing the dependencies among the quantities of interest. For example, it shows that the primary side self impedance (Z_{11}) has a nonzero real part in the presence of a FO, which increases with stronger coupling to the object.

Apart from proposing an extended model to account for realistic channel effects, the collected data of the WPT channel for a variety of usage scenarios have been stored in a database. These frequency-dependent Z-parameter data can be easily integrated with a circuit simulator for link and system level studies of in-band communications at the frequency range of interest. For example, the Qi Specification employs frequency shift keying (FSK) modulation for the forward communication link (power transmitter to receiving device), and the measured channel can be used to investigate the impact of different channel effects (e.g., without and with FOs) on the bit error rate for a given transceiver architecture.

5.2 Possible Future Work

To improve on the results, similar measurements can be done with more accurate and well calibrated equipment. A better characterization of the WPT coil-to-coil channel would require more measurement accuracy in the calculation of the real parts of the Z-parameters, and thus further investigations into the equipment required to achieve this would be required. Part of this effort could be directed to performing further analysis of the sensitivity of the real parts of the Z-parameters, and to what extent they are affected by noise and measurement error.

A further look into power loss due to eddy currents is also an interesting aspect for future work, both for cases with FOs, as well as with ferrite shielding. It could be investigated how well, and if, eddy currents induced in objects near the WPT channel can be modeled and parameterized as virtual coils using knowledge of material properties, such as resistivity and permeability, of the nearby object(s).

Beside a deterministic approach, another approach common to wireless com-

munication channel modeling is statistical modeling. For example, based on a pool of channel data, some statistics (typically second order statistics) can be extracted to capture the characteristics of the channel in a statistical sense. This approach facilitates a more compact representation of the channel, and it may also lead to a better understanding of the underlying physics of the channel. Since channel data have already been collected, some standard statistical channel modeling techniques can be applied to extract the parameters of some statistical WPT channel models.

References

[1] S. Chatterjee, "Michael Faraday: Discovery of electromagnetic induction," *Resonance*, vol. 7, no. 3, pp. 35–45, 2002.

[2] M. Christiano, *Tesla's Towers: Pikes Peak, Wardenclyffe, and Wireless Power Transmission*, All About Circuits, 2016. Accessed on: July 02, 2019 [Online]. Available: https://www.allaboutcircuits.com/technical-articles/teslas-towers-pikes-peak-wardenclyffe-and-wireless-power-transmission/.

[3] D. Schatz, *Wireless Power For Medical Devices*, MDDI Online, 2013. Accessed on: July 02, 2019 [Online] Available at: https://www.mddionline.com/wireless-power-medical-devices

[4] *Which Phones Support Qi Wireless Charging?*, Nonstop, 2018. Accessed on: Nov 04, 2019 [Online] Available: https://www.nonstopproducts.com/blog/2018/12/12/which-phones-support-qi-wireless-charging

[5] *The Qi Wireless Power Transfer System Power Class 0 Specification, Version 1.2.4*, Wireless Power Consortium, Feb. 2018

[6] Wireless Power Consortium homepage. Accessed on: July 02, 2019 [Online] Available: http://www.wirelesspowerconsortium.com

[7] V. Muratov, "Methods for Foreign Object Detection in Inductive Wireless Charging," 2017. Accessed on: Aug. 17, 2019. [Online]. Available: https://www.wirelesspowerconsortium.com/data/downloadables/1/9/0/9/wpc1704-vladimir-muratov-methods-for-foreign-object-detection.pdf

[8] D. K. Cheng, *Field and Wave Electromagnetics: Pearson New International Edition*, 2nd ed. Pearson Education Limited, 2013, ch. 6.

[9] D. K. Cheng, *Field and Wave Electromagnetics: Pearson New International Edition*, 2nd ed. Pearson Education Limited, 2013, ch. 7.

[10] W. Benenson, J. W. Harris, H. Stöcker, H. Lutz, *Handbook of Physics*. New York: Springer-Verlag, 2002, pp. 492.

[11] M. W. Baker and R. Sarpeshkar, "Feedback Analysis and Design of RF Power Links for Low-Power Bionic Systems," in *IEEE Transactions on Biomedical Circuits and Systems*, vol. 1, no. 1, pp. 28-38, March 2007.

[12] B. Evstatiev, Class Lecture, "Mutually Coupled Inductors. Coupling Coefficient. Power and Energy of Mutually Coupled Inductors. Analysis of Circuits with Mutually Coupled Inductor." Accessed on: Aug. 17, 2019. [Online]. Available: https://www.uni-ruse.bg/disciplines/TE/Lecturenotes/LecturesnotesMutuallycoupledinductors.pdf

[13] D. R. Choudhury, *Networks and Systems*. New Delhi: New Age International Publishers, 1998, ch. 10.

[14] *Using a Network Analyzer to Characterize High-Power Components*, Agilent. Accessed on: Aug. 25, 2019. [Online]. Available: https://www.testworld.com/wp-content/uploads/using-a-network-analyzer-to-characterize-high-power-components.pdf

[15] *LPA05 Laboratory Amplifier User Guide*, Newtons4th Ltd, Leicaster, United Kingdom. Accessed on: Aug. 19, 2019. [Online]. Available: https://www.newtons4th.com/wp-content/uploads/2014/05/LPA05-user-guide-v15-1.pdf

[16] B. Hesterman, "Analysis and Modeling of Magnetic Coupling," Discovery Learning Center, University of Colorado, Boulder, Colorado, 2014.

Appendix A

Current and Voltages in the extended FHA model

The following expressions for currents and voltages in the extended FHA model, discussed in Section 2.6, are obtained through substitution of the virtual coil currents, (2.15) and (2.16), into the expressions for primary and secondary coil voltage and currents, (2.12), (2.13) and (2.14).

$$
\begin{aligned}
I_1 = V_{IN}\Big[& -2j\omega^3 M_{23}M_{24}M_{34} + \omega^2(Z_4M_{23}^2 + Z_3M_{24}^2 + Z_2M_{34}^2) + Z_2Z_3Z_4\Big] \\
& \Big/\Big[\omega^4(M_{12}^2M_{34}^2 + M_{14}^2M_{23}^2 + M_{13}^2M_{24}^2 \\
& - 2M_{12}M_{13}M_{24}M_{34} - 2M_{12}M_{14}M_{23}M_{34} - 2M_{13}M_{14}M_{23}M_{24}) \\
& + j\omega^3(-2M_{12}M_{13}M_{23}Z_4 - 2M_{12}M_{14}M_{24}Z_3 \\
& - 2M_{13}M_{14}M_{34}Z_2 - 2M_{23}M_{24}M_{34}Z_1) \\
& + \omega^2(Z_3Z_4M_{12}^2 + Z_2Z_4M_{13}^2 + Z_2Z_3M_{14}^2 + Z_1Z_4M_{23}^2 + Z_1Z_3M_{24}^2 + Z_1Z_2M_{34}^2) \\
& + Z_1Z_2Z_3Z_4\Big] \quad [\mathrm{A}]
\end{aligned}
\tag{A.1}
$$

$$
\begin{aligned}
I_2 = & -V_{IN}\Big[j\omega^3(M_{12}M_{34}^2 - M_{34}M_{13}M_{24} - M_{34}M_{14}M_{23}) \\
& + \omega^2(M_{13}M_{23}Z_4 + M_{14}M_{24}Z_3) + j\omega M_{12}Z_3Z_4\Big] \\
& \Big/\Big[\omega^4(M_{12}^2M_{34}^2 - 2M_{12}M_{13}M_{24}M_{34} - 2M_{12}M_{14}M_{23}M_{34} \\
& + M_{13}^2M_{24}^2 - 2M_{13}M_{14}M_{23}M_{24} + M_{14}^2M_{23}^2) \\
& + 2j\omega^3(-M_{12}M_{13}M_{23}Z_4 - M_{12}M_{14}M_{24}Z_3 \\
& - M_{13}M_{14}M_{34}Z_2 - M_{23}M_{24}M_{34}Z_1) \\
& + \omega^2(Z_3Z_4M_{12}^2 + Z_2Z_4M_{13}^2 + Z_2Z_3M_{14}^2 + Z_1Z_4M_{23}^2 + Z_1Z_3M_{24}^2 + Z_1Z_2M_{34}^2) \\
& + Z_1Z_2Z_3Z_4\Big] \quad [\mathrm{A}]
\end{aligned}
\tag{A.2}
$$

$$
\begin{aligned}
V_1 = V_{IN} + V_{IN}\Big[&(L_P\omega + Z_1 j - jR_P) \\
&\cdot \Big\{2\omega^3 M_{23}M_{24}M_{34} + j\omega^2(Z_4M_{23}^2 + Z_3M_{24}^2 + Z_2M_{34}^2) + jZ_2Z_3Z_4\Big\}\Big] \\
&\Big/\Big[\omega^4(M_{12}^2M_{34}^2 - 2M_{12}M_{13}M_{24}M_{34} - 2M_{12}M_{14}M_{23}M_{34} \\
&+ M_{13}^2M_{24}^2 - 2M_{13}M_{14}M_{23}M_{24} + M_{14}^2M_{23}^2) \\
&- 2j\omega^3(M_{12}M_{13}M_{23}Z_4 + M_{12}M_{14}M_{24}Z_3 + M_{13}M_{14}M_{34}Z_2 + M_{23}M_{24}M_{34}Z_1) \\
&+ \omega^2(Z_3Z_4M_{12}^2 + Z_2Z_4M_{13}^2 + Z_2Z_3M_{14}^2 \\
&+ Z_1Z_4M_{23}^2 + Z_1Z_3M_{24}^2 + Z_1Z_2M_{34}^2) + Z_1Z_2Z_3Z_4\Big] \quad [\mathrm{V}]
\end{aligned}
\tag{A.3}
$$

$$
\begin{aligned}
V_2 = V_{IN}\cdot\omega\Big[&(R_S - Z_2 + j\omega L_S) \\
&\cdot \Big\{j\omega^2(M_{13}M_{24}M_{34} + M_{14}M_{23}M_{34} - M_{12}M_{34}^2) \\
&- \omega(M_{13}M_{23}Z_4\omega + M_{14}M_{24}Z_3\omega) - jM_{12}Z_3Z_4\Big\}\Big] \\
&\Big/\Big[\omega^4(M_{12}^2M_{34}^2 - 2M_{12}M_{13}M_{24}M_{34} - 2M_{12}M_{14}M_{23}M_{34} \\
&+ M_{13}^2M_{24}^2 - 2M_{13}M_{14}M_{23}M_{24} + M_{14}^2M_{23}^2) \\
&- 2j\omega^3(M_{12}M_{13}M_{23}Z_4 + M_{12}M_{14}M_{24}Z_3 + M_{13}M_{14}M_{34}Z_2 + M_{23}M_{24}M_{34}Z_1) \\
&+ \omega^2(Z_3Z_4M_{12}^2 + Z_2Z_4M_{13}^2 + Z_2Z_3M_{14}^2 \\
&+ Z_1Z_4M_{23}^2 + Z_1Z_3M_{24}^2 + Z_1Z_2M_{34}^2) + Z_1Z_2Z_3Z_4\Big] \quad [\mathrm{V}]
\end{aligned}
\tag{A.4}
$$

Printed by Tryckeriet i E-huset, Lund 2020

LUND
UNIVERSITY

Series of Master's theses
Department of Electrical and Information Technology
LU/LTH-EIT 2020-750
http://www.eit.lth.se